Parameterization methods of atmospheric upward and downward radiation fluxes in visible and near-infrared bands

YANG Guijun[1, 2], GAO Zhongling[1, 3], HUANG Wenjiang[1], LIU Qiang[1], WANG Jihua[1], ZHANG Mingyue[1]

1. *National Engineering Research Center for Information Technology in Agriculture*, *Beijing Academy of Agriculture and Forestry Sciences*, *Beijing* 100097, *China*;
2. *State Key Laboratory of Remote Sensing Science*, *Institute of Remote Sensing Applications*, *Chinese Academy of Sciences*, *Beijing* 100101, *China*;
3. *School of Geography and Remote Sensing Science*, *Beijing Normal University*, *Beijing* 100875, *China*

Abstract: Atmospheric upward and downward radiations in visible and near-infrared bands are the key input parameters for radiative transfer modeling, imaging simulation and atmospheric correction. This study presents the numeral models and computing methods of the atmospheric parameters which are related to the two parameters according to four-stream radiative transfer theory. Focusing on the six bands of Landsat 5 TM, the parametric models among atmospheric parameters, water vapor content, visibility distance and solar incidence zenith angle were designed, based on which the sensitivity of each parameter is analyzed. The results showed that the parametric models have higher precision. Meanwhile, the atmospheric upward and downward diffuse radiation of each band for TM remote sensing was calculated and the changes under the coverage of vegetation and bare soil were analyzed.

Key words: atmospheric upward and downward radiation, radiation transfer, atmospheric correction, parametric model

CLC number: TP722.5/P407 **Document code:** A

Citation format: Yang G J, Gao Z L, Huang W J, Liu Q, Wang J H and Zhang M Y. 2010. Parameterization methods of atmospheric upward and downward radiation fluxes in visible and near-infrared bands. *Journal of Remote Sensing*. **14**(4): 637—662

1 INTRODUCTION

The effects of the atmosphere on solar radiation are mainly reflected in scattering and absorption. The solar radiation becomes weak with the scattering and absorption of aerosol particles and water molecules in the atmosphere, meanwhile, part of the scattering and downward solar radiation into the sensor make the atmospheric background and the ground surface information mix together, and limit the quantitative application of remote sensing data. In the past few years, the issue as to how to establish an effective atmospheric radiative transfer model and achieve accurate atmospheric correction of remote sensing data has become a focus of research. Through large amounts of atmospheric scientists' hard work for over 30 years, the atmospheric radiative transfer model calculated by wide/arrow spectral bands and by every spectral line has been successfully developed. These transfer models concern various kinds of observation method, which are suitable for a wide range of the electromagnetic spectrum and various variable meteorological elements. In the present atmospheric radiative transfer models (e.g. 6S, LOWTRAN, MODTRAN and FASCODE), a large number of detailed atmospheric parameters should be inputted, furthermore, direct results of the atmospheric radiation fluexs can not be obtained. Based on the above situations, the commercial tools for atmospheric correction, for example, ATCOR, FLAASH and ACORN, etc., have been developed, which also require the detailed input parameters. Currently, the researchers have designed various simplified atmospheric radiative transfer model according to the specific sensor load and needs. For example, Liang *et al.*(2001, 2004), Ghulam *et al.*(2004), Nie *et al.*(2007) divided the sensor radiation at entrance pupil into two items (Kaufman & Sendra, 1988; Vermote *et al.*, 2002), namely the atmospheric path radiation and the solar direct radiation after multiple scattering by ground surface and BOA (bottom of the atmosphere) into the sensor. Through changing the land surface albedo conditions and the height of sensor, atmospheric path radiation (L_0), total solar downward radiation (F_d), atmospheric hemisphere albedo (S) and the transmittance (T_μ) between ground object and sensor were calculated under the condition of the given atmospheric condition and the observation

Received: 2009-07-30; **Accepted**: 2009-12-15

Foundation: Natural Science Foundation of China (No. 40901173), Beijing Natural Science Foundation(No. 4102021) and Open Funds of State Key Laboratory of Remote Sensing Science, Jointly Sponsored by the Institute of Remote Sensing Applications of Chinese Academy of Sciences and Beijing Normal University(No. 2009KFJJ020) and National Department Public Benefit Research Foundation of China(No. 200803037).

First author biography: YANG Guijun(1976—), male, research assistant. His research interests cover radiative transfer modelling, imagery simulation, atmospheric correction, quantitative inversion and land cover change monitoring. E-mail: guijun.yang@163.com

geometry among sun-ground object-sensor by means of the MODTRAN model. Meanwhile, the corresponding look-up table was built up. The contribution of upward and downward diffuse radiation to the sensor radiation at entrance pupil was not considered in the methods above, but actually, the radiation from ground surface contains not only the direct solar radiation by the surface objects, but also the atmospheric upward diffuse radiation scattered by neighboring objects and atmospheric downward diffuse radiation by the reflection of surface objects. Therefore, without considering the contribution of the latter two parts, there exists a certain degree of deficiency on the atmospheric correction, that is, the atmospheric condition of the obtained atmospheric parameter is better than the real atmospheric condition. In addition, most scholars tend to consider the process of surface–atmospheric radiative transfer coupling as a whole during the process of ground surface radiative transfer modeling. For example, in the three-dimensional radiative transfer models of RGM, DART, etc. (Qin & Gerstl, 2000; Gastellu-Etchegorry *et al.*, 2004), the atmospheric upward and downward radiative values for the given spectral band should be provided. Thus, quantitative calculation on atmospheric upward and downward radiation fluxes is still a problem to be solved.

In this paper, the numeral model of atmospheric radiative transfer was established based on the four–stream radiative transfer theory (Verhoef, 1984), and the computing method of atmospheric upward and downward diffuse radiation fluxes was discussed. Meanwhile, the radiation components were parameterized according to the key factors of water vapor content, visible and solar incidence zenith angle, and then the direct, rapid, accurate calculation on atmospheric upward and downward radiation flux was successfully achieved. Finally, based on this, the computing result of the narrow-band radiation fluxes was obtained combining with the data of Landsat 5 TM.

2 ESTABLISHMENT OF ATMOSPHERIC RADIATIVE TRANSFER NUMERAL MODEL

The basic idea of the parametric method is: (1) The numeral model of atmospheric radiative transfer with atmospheric upward and downward radiation components should be established. And the two components should be separated from the sensor radiation at entrance pupil. (2) Based on 6S, MODTRAN model (Kaufman & Sendra, 1988; Berk *et al.*, 2000; Vermote *et al.*, 2002). the numeral model could be solved, from which the atmospheric upward and downward radiation fluxes during visible – near infrared spectral band (0.4—2.5μm) could be obtained. (3) Based on the key atmospheric factors of visible–near infrared band which has influence on the atmospheric radiative transfer, the parametric model is established by performing multiple non-linear regression analysis on the atmospheric upward and downward radiation fluxes.

In the spectral range of visible–near infrared band, the received radiation of sensor is mainly from the reflection of solar radiation. The four-stream approximation of the interaction between the radiation received by the sensor and the atmosphere is shown in Fig. 1. In order to ensure the consistence of nomenclature of the four–stream approximation expression, the following symbolic variables are defined: ρ represents the scattering process associated with the atmosphere; τ represents the transmittance through a layer, either directly or via (forward) scattering; r represents the directional reflection corresponding to ground surface; the subscript s indicates incidence direction of the solar rays; the subscript d indicates the direction of upward or downward hemispherical diffuse; the subscript o indicates observation direction of sensor ; b, t are the height of the bottom atmosphere and top atmosphere.

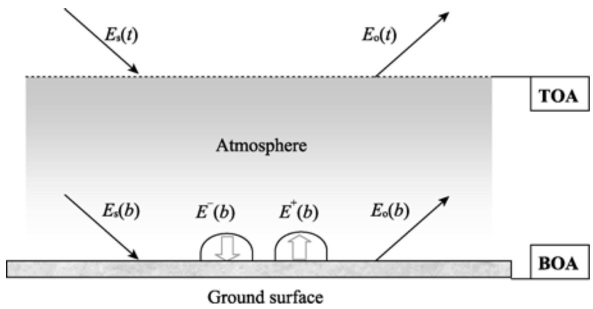

Fig. 1 Diagram of the atmospheric radiative transfer process

Based on the four-stream atmospheric radiative transfer theory, the fluxes related to the atmospheric radiative transfer are described as the following equations:

$$E_s(b) = \tau_{ss} E_s(t) \tag{1}$$

$$E^-(b) = \tau_{sd} E_s(t) + \rho_{dd} E^+(b) \tag{2}$$

$$E^+(b) = \overline{r_{sd}} E_s(b) + \overline{r_{dd}} E^-(b) \tag{3}$$

$$E_o(b) = r_{so} E_s(b) + r_{do} E^-(b) \tag{4}$$

$$E_o(t) = \rho_{so} E_s(t) + \tau_{do} E^+(b) + \tau_{oo} E_o(b) \tag{5}$$

where $E_s(t)$ is solar incidence radiation flux at TOA (top of the atmosphere); $E_s(b)$ is direct solar radiation flux at BOA (bottom of the atmosphere); $E^+(b)$ and $E^-(b)$ respectively represents skylight diffuse upward and downward radiation; $E_o(b)$ is the total surface radiation in the observation direction; $E_o(t)$ is the total radiation at TOA in the observation direction; τ_{ss} is direct transmittance of solar ray through the whole atmospheric layer; τ_{sd} is the diffuse transmittance in the direction of solar rays-hemisphere; τ_{do} is diffuse transmittance from hemisphere to the observation direction of sensor; τ_{oo} is the direct transmittance from surface to the observation direction; ρ_{dd} is the spherical albedo of the atmosphere at BOA; ρ_{so} is atmospheric bidirectional reflectance at TOA; $\overline{r_{sd}}$ is the average surroundings diffuse reflectance for solar incidence; $\overline{r_{dd}}$ is the average surroundings diffuse reflectance for diffuse incidence; r_{so} is the ground surface bidirectional reflectance; r_{do} is reflectance in the hemispheric–observation direction.

Apparent reflectance $r_{p,\lambda}$ at TOA can be obtained by simultaneously solving the equations developed above:

$$
\begin{aligned}
r_{p,\lambda} = \rho_{\mathrm{so},\lambda} + & \quad \text{(a)} \\
\tau_{\mathrm{do},\lambda}\frac{(\overline{r_{\mathrm{sd},\lambda}}\tau_{\mathrm{ss},\lambda} + \overline{r_{\mathrm{dd},\lambda}}\tau_{\mathrm{sd},\lambda})}{1-\overline{r_{\mathrm{dd},\lambda}}\rho_{\mathrm{dd},\lambda}} + & \quad \text{(b)} \\
\tau_{\mathrm{oo},\lambda}r_{\mathrm{do},\lambda}\frac{(\tau_{\mathrm{sd},\lambda} + \tau_{\mathrm{ss},\lambda}\overline{r_{\mathrm{sd},\lambda}}\rho_{\mathrm{dd},\lambda})}{1-\overline{r_{\mathrm{dd},\lambda}}\rho_{\mathrm{dd},\lambda}} + & \quad \text{(c)} \\
\tau_{\mathrm{oo},\lambda}r_{\mathrm{so},\lambda}\tau_{\mathrm{ss},\lambda} & \quad \text{(d)}
\end{aligned}
\tag{6}
$$

where, (a), (b), (c) and (d) indicate single scattered radiation, atmospheric upward diffuse radiation, atmospheric downward diffuse radiation and the direct solar radiation reflected by ground surface contributing to the total sensor radiation at entrance pupil, respectively.

Similarly, the following equations can be set up through establishing Eq.(1) — Eq.(3) simultaneously:

$$E^{+}(b) = \frac{(\overline{r_{\mathrm{sd}}}\tau_{\mathrm{ss}} + \overline{r_{\mathrm{dd}}}\tau_{\mathrm{sd}})}{1-\overline{r_{\mathrm{dd}}}\rho_{\mathrm{dd}}}E_{\mathrm{s}}(t) \tag{7}$$

$$E^{-}(b) = \frac{(\tau_{\mathrm{sd}} + \tau_{\mathrm{ss}}\overline{r_{\mathrm{sd}}}\rho_{\mathrm{dd}})}{1-\overline{r_{\mathrm{dd}}}\rho_{\mathrm{dd}}}E_{\mathrm{s}}(t) \tag{8}$$

Further:

$$Q = \frac{E^{+}(b)}{E^{-}(b)} = \frac{(\overline{r_{\mathrm{sd}}}\tau_{\mathrm{ss}} + \overline{r_{\mathrm{dd}}}\tau_{\mathrm{sd}})}{(\tau_{\mathrm{sd}} + \tau_{\mathrm{ss}}\overline{r_{\mathrm{sd}}}\rho_{\mathrm{dd}})} \tag{9}$$

It can been seen that atmospheric downward and upward radiation in the spectral range of visible-near infrared band are affected by solar incidence angle, atmospheric condition and surface conditions, which is independent of the observation direction. To figure out the upward and downward radiation and the ratio of them, the atmospheric and environment property parameters in the equations should be obtained in advance. Assuming the ground surface as homogeneous Lambertian, surface albedo is defined as the constant value α_λ at wavelength λ (Surface albedo indicates the ratio of the reflection flux of solar incidence radiation to the solar incidence radiation flux), which then substitutes the variables corresponding to surface reflection in the equation, as follows:

$$Q = \frac{E^{+}(b)}{E^{-}(b)} = \frac{\alpha_\lambda(\tau_{\mathrm{ss},\lambda} + \tau_{\mathrm{sd},\lambda})}{(\tau_{\mathrm{sd},\lambda} + \tau_{\mathrm{ss},\lambda}\alpha_\lambda\rho_{\mathrm{dd},\lambda})} \tag{10}$$

3 PARAMETERIZATION OF THE ATMOSPHERIC UPWARD AND DOWNWARD RADIATION FLUX

3.1 Computing method of atmospheric radiation flux

MODTRAN (moderate resolution atmospheric transmittance and radiance code) compiled by FORTRAN language was developed by Spectra Technology, Inc. United States and Air Force Physics Laboratory. It is suitable for the computation of atmospheric transfer radiation within the spectral range of 0.2μm—∞ (Berk *et al.*, 2000). Since 1989, MODTRAN has gradually been integrated with the latest achievements in atmospheric radiative transfer, and the newest version is 4.0. MODTRAN 4.0 improves the computing precision of Rayleigh scattering and complex refractive index, incorporated DISORT for the solution of radiative transfer model by multi–stream approximation, and introduced various BRDF models to make possible the parameterized input of surface characteristics. Several basic databases in MODTRAN have been updated, and the processing method of the upper atmosphere is improved. MODTRAN is one of the most popularly used radiative transfer models with higher precision (Aires *et al.*, 2002; Ellicott *et al.*, 2009; Verhoef & Bach, 2003).

The three atmospheric parameters $\tau_{\mathrm{ss},\lambda}$, $\tau_{\mathrm{sd},\lambda}$ and $\rho_{\mathrm{dd},\lambda}$ in $E^{+}(b)$, $E^{-}(b)$ and Q can be obtained through Eq. (6) and the output of MODTRAN model. Assuming the ground surface as homogeneous Lambertian, Eq. (6) is changed into another form, shown as follows:

$$
\begin{aligned}
r_{p,\lambda} = \rho_{\mathrm{so},\lambda} + & \quad \text{(a)} \\
\tau_{\mathrm{do},\lambda}\alpha_\lambda\frac{(\tau_{\mathrm{ss},\lambda} + \tau_{\mathrm{sd},\lambda})}{1-\alpha_\lambda\rho_{\mathrm{dd},\lambda}} + & \quad \text{(b)} \\
\tau_{\mathrm{oo},\lambda}\alpha_\lambda\frac{(\tau_{\mathrm{sd},\lambda} + \tau_{\mathrm{ss},\lambda}\alpha_\lambda\rho_{\mathrm{dd},\lambda})}{1-\alpha_\lambda\rho_{\mathrm{dd},\lambda}} + & \quad \text{(c)} \\
\tau_{\mathrm{oo},\lambda}\alpha_\lambda\tau_{\mathrm{ss},\lambda} & \quad \text{(d)}
\end{aligned}
\tag{11}
$$

Set α_λ as 0, 50% and 100%, respectively, and input the atmospheric parameters of MODTRAN 4 model based on meteorological observation data and the three atmospheric parameters will be obtained after three calculation results. To make the output results of MODTRAN 4 model convenient for solving the equations, radiation flux related to (a), (b), (c) and (d) are saved directly as a single file through modifying the program of MODTRAN 4 model. The relationship among column data identification of tape7 file as the output of MODTRAN, variables in MODTRAN 4 and Eq.(6) are respectively described as: (1) The sum of reflectance radiation at TOA and the total atmospheric upward diffuse radiation is 'SOL SCAT' →'SUMSSR'→(a)+(b). (2) The direct solar radiation reflected by ground surface is 'DRCT RFLT' →'RFLSS'→(d). (3) The sum of direct solar reflected by surface and the atmospheric downward diffuse radiation is 'GRND RFLT'→'RFSURF'→ (c)+(d). The following equations can be obtained according to the relationship described above:

$$L_{(a)+(b)} = \left[\rho_{\mathrm{so},\lambda} + \tau_{\mathrm{do},\lambda}\alpha_\lambda\frac{(\tau_{\mathrm{ss},\lambda} + \tau_{\mathrm{sd},\lambda})}{1-\alpha_\lambda\rho_{\mathrm{dd},\lambda}}\right]\frac{E_{\mathrm{s}}(t)}{\pi}\cos\theta_{\mathrm{s}} \tag{12}$$

$$L_{(c)+(d)} = \left[\tau_{\mathrm{oo},\lambda}\alpha_\lambda\frac{(\tau_{\mathrm{sd},\lambda} + \tau_{\mathrm{ss},\lambda})}{1-\alpha_\lambda\rho_{\mathrm{dd},\lambda}}\right]\frac{E_{\mathrm{s}}(t)}{\pi}\cos\theta_{\mathrm{s}} \tag{13}$$

$$L_{(d)} = \tau_{\mathrm{oo},\lambda}\alpha_\lambda\tau_{\mathrm{ss},\lambda}\frac{E_{\mathrm{s}}(t)}{\pi}\cos\theta_{\mathrm{s}} \tag{14}$$

where $L_{(a)+(b)}$, $L_{(c)+(d)}$ and $L_{(d)}$ indicate the radiation flux value components obtained by MODTRAN 4 model at wavelength λ.

(1) Assume that the direct transmittance $\tau_{\mathrm{oo},\lambda}$ and $\tau_{\mathrm{ss},\lambda}$ satisfy the Beer's Law, the following equation would be established:

$$\tau_{\mathrm{oo},\lambda} = \exp(-b/\cos\theta_{\mathrm{o}}), \tau_{\mathrm{ss},\lambda} = \exp(-b/\cos\theta_{\mathrm{s}}) \tag{15}$$

where b is the atmospheric optical thickness of the whole atmosphere, θ_{o} is observation zenith angle, θ_{s} is solar incidence zenith angle. The application of Beer's Law will generally achieve high accuracy within the atmospheric window wave band, except in the strong water vapor absorption band which may lead to large error. The following equations can be established through Eq.(14) and Eq. (15) when α_λ =100%:

$$\begin{aligned}\tau_{\mathrm{oo},\lambda}\tau_{\mathrm{ss},\lambda} &= \exp[-b(1/\cos\theta_{\mathrm{s}}+1/\cos\theta_{\mathrm{o}})] \\ &= L_{(d)}{}^{100}\times\pi/(E_{\mathrm{s}}(t)\cos\theta_{\mathrm{s}})\end{aligned} \quad (16)$$

The following formula can be obtained:

$$b=-\ln[L_{(d)}{}^{100}\times\pi/(E_{\mathrm{s}}(t)\cos\theta_{\mathrm{s}})]/(1/\cos\theta_{\mathrm{s}}+1/\cos\theta_{\mathrm{o}}) \quad (17)$$

$\tau_{\mathrm{ss},\lambda}$ can be directly solved with b and Eq. (15).

(2) The Eq. (13) can be changed into the following forms when α_λ=50% and α_λ=100%:

$$\begin{cases}\tau_{\mathrm{oo},\lambda}0.5\dfrac{(\tau_{\mathrm{sd},\lambda}+\tau_{\mathrm{ss},\lambda})}{1-0.5\rho_{\mathrm{dd},\lambda}}=L_{(c)+(d)}{}^{50}\times\pi/(E_{\mathrm{s}}(t)\cos\theta_{\mathrm{s}}) \\ \tau_{\mathrm{oo},\lambda}\dfrac{(\tau_{\mathrm{sd},\lambda}+\tau_{\mathrm{ss},\lambda})}{1-\rho_{\mathrm{dd},\lambda}}=L_{(c)+(d)}{}^{100}\times\pi/(E_{\mathrm{s}}(t)\cos\theta_{\mathrm{s}})\end{cases} \quad (18)$$

$\rho_{\mathrm{dd},\lambda}$ can be directly solved as:

$$\rho_{\mathrm{dd},\lambda}=\frac{L_{(c)+(d)}{}^{100}-2\times L_{(c)+(d)}{}^{50}}{L_{(c)+(d)}{}^{100}-L_{(c)+(d)}{}^{50}} \quad (19)$$

(3) The following equation can be set up through establishing Eq. (13) and Eq.(14) simultaneously when α_λ=100%:

$$\tau_{\mathrm{sd},\lambda}=[L_{(c)+(d)}{}^{100}(1-\rho_{\mathrm{dd},\lambda})/L_{(d)}{}^{100}-1]\tau_{\mathrm{ss},\lambda} \quad (20)$$

3.2 Analysis of the atmospheric radiation flux

When performing the atmospheric correction of MODIS data in the spectral range of visible–mid infrared band (Vermote *et al.*, 2002), high accuracy can be achieved through simplified mutual coupling model of water vapor absorption and aerosol scattering. In a short period of time, effects of the atmosphere on short-wave radiation are mainly from water vapor content and aerosol conditions; whereas other gases and trace gases change slightly, which have relatively stable effect on the process of radiative transfer. Through the analysis of neighboring effect on atmospheric radiative transfer, it also can be concluded that the main atmospheric factors influencing on neighboring effect are water vapor content and visibility (Yang *et al.*, 2007, 2008, 2009). Of course, solar incidence zenith angle is the main geometric factor effecting on the length of atmospheric radiation path in the spectral range of visible–near infrared band. Statistical analysis on the change of water vapor content within gas column is performed with the data of 1413 atmospheric profiles in clear sky conditions stored in the TIGR atmospheric profile database. The change range of water vapor content is from 0.0 to 8.0 g/cm^2, and the water vapor content of 60% of the profiles is around 1.0(g/cm^2); the atmospheric visibility distance ranges from 0.1 to 35 km, with reference to Liang *et al*. (2001); solar incidence zenith angle ranges from 0 to 70° determined by Landsat 5 satellite overpass time and the geographical position. Based on the standard atmosphere model in U.S. in 1976, specific parameters are set as shown in Table 1, and statistical analysis is performed by changing the three variables of water vapor content, visibility distance and solar incidence zenith angle; here, the observation direction is top-down vertical direction, and the default parameter values are 1.0 g/cm^2 of water vapor content, 25.0 km of visibility distance and 30.0° of solar incidence zenith angle.

Table 1 The settings of input atmospheric parameters

Water vapor content /(g/cm^2)	Visibility distance /km	Solar incidence zenith angle /(°)
1.0	0.1	0.0
2.0	0.5	10.0
3.0	1.0	20.0
4.0	5.0	**30.0**
5.0	10.0	40.0
6.0	15.0	50.0
7.0	**25.0**	60.0
8.0	35.0	70.0

3.2.1 Computing results of parameters with different water vapor content

The main absorption centers of water vapor in the atmosphere include the wavelength of 0.94, 1.1, 1.38 and1.87μm. It can be seen from Fig.2 that the change of the three atmospheric parameters caused by different water vapor content is not obvious, even if the water vapor content dynamic ranges from 1.0—8.0g/cm^2. The three atmospheric parameters slightly decrease with the increase of water vapor content, and the variation range is only within round 5%. The reason is that, except for the water absorbing zone, water vapor in atmosphere has slight Rayleigh scattering only within the long wavelength (>1.0 μm), and half of solar energy is absorbed in near-infrared band. Water vapor absorption zone mainly concentrates on thermal infrared band, and there is more absorption under conditions of higher water vapor content. Therefore, water vapor content is the most important influencing factors in thermal infrared remote sensing but less important in visible-infrared band. In the figure, the downward arrow indicates a negative correlation with water vapor increase, while the upward Arrow indicates a positive correlation. The meanings of arrows in the following figures are the same.

3.2.2 Computing results of different aerosol visibility

Mie scattering by aerosol in visible-near infrared band is very obvious. The extinction distance of the surface aerosol at 550nm ranges from 39.1 to 0.1 km^{-1} when the atmospheric visibility distance changes in the range of 0.1—35.0 km, which leads to the largest change range of corresponding atmospheric parameters up to 10 times of the original, as shown in Fig.3, where $\tau_{\mathrm{ss},\lambda}$ and $\tau_{\mathrm{sd},\lambda}$ rise with the increase of visibility distance, but $\rho_{\mathrm{dd},\lambda}$ decreases. The reason is that the probability of multi-scattering by aerosol is reduced with the increase of visibility distance, which directly leads to the increase of the whole layer atmospheric direct and diffuse transmittance. But the probability of multiple scattering in hemisphere-hemisphere direction among atmospheric upward and downward diffuse radiation is reduced, which leads to the decline of $\rho_{\mathrm{dd},\lambda}$.

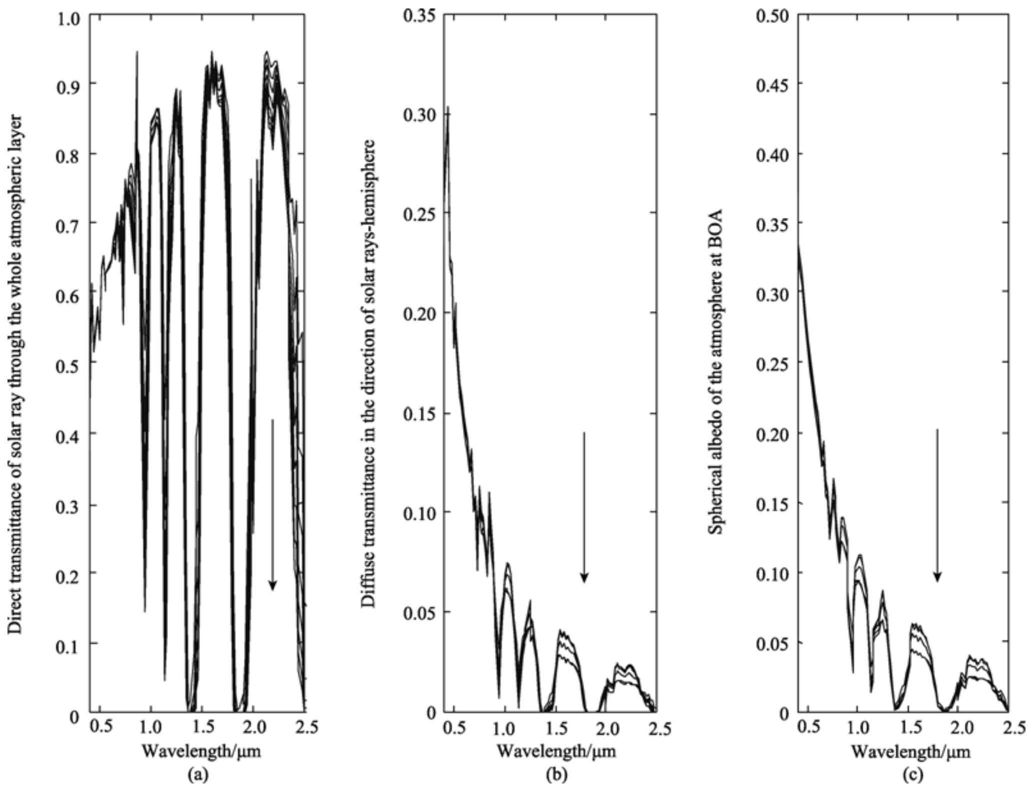

Fig. 2 Results of three atmospheric parameters in different water vapor content
(a) Direct transmittance of solar ray through the whole atmospheric layer; (b) Diffuse transmittance in the direction of solar rays-hemisphere; (c) Spherical albedo of the atmosphere at BOA

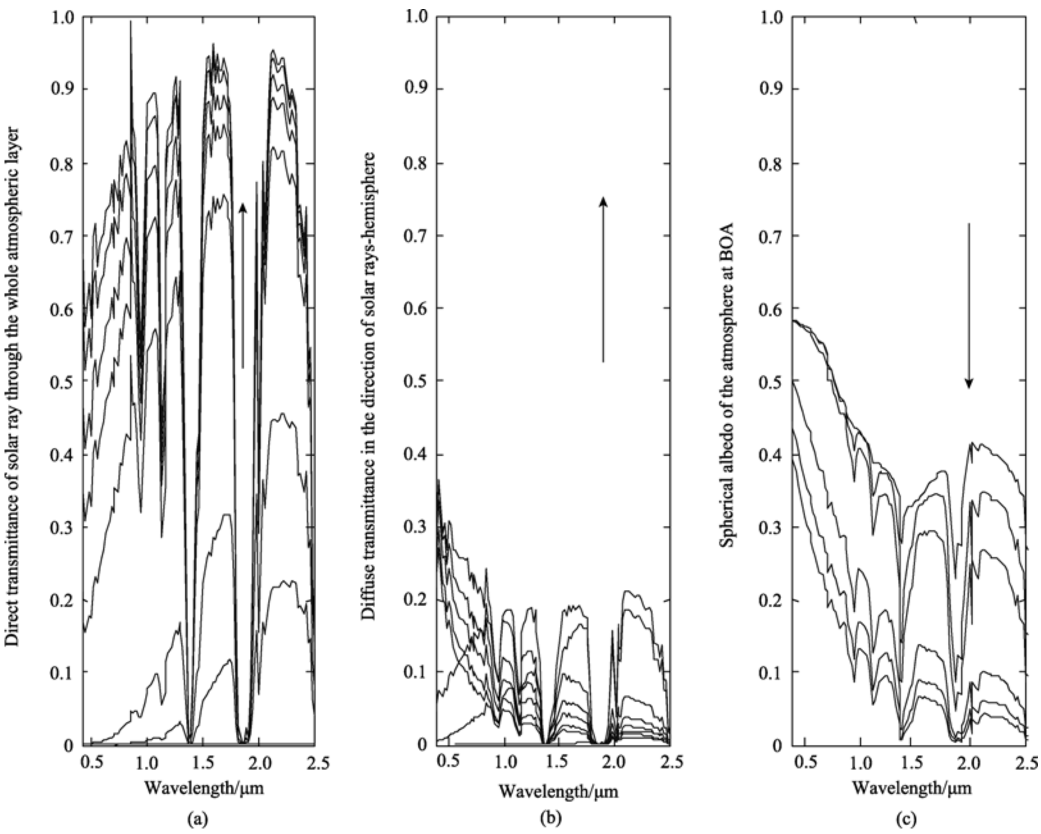

Fig. 3 Results of three atmospheric parameters in different meteorology visibility distance
(a) Direct transmittance of solar ray through the whole atmospheric layer; (b) Diffuse transmittance in the direction of solar rays-hemisphere; (c) Spherical albedo of the atmosphere at BOA

3.2.3 Calculation results of different solar incidence zenith angle

While the solar incidence zenith angle changes from 0 to 70°, solar rays transmission distance through the atmosphere will be increased, where $\tau_{ss,\lambda}$ gradually declines with the increase of the angle, and the change range is up to 10 times, as shown in Fig.4. The change of solar incidence zenith angle has significantly impact on the direct light transmittance. On the contrary, $\tau_{sd,\lambda}$ increases with the angle, of which the range is small. While $\rho_{dd,\lambda}$ is independent of the solar incidence zenith angle, it keeps constant. The reason is that with the increase of zenith angle and direct light transmission path through the atmosphere, the probability of multi-scattering during transmission has a certain increase, but multi-scattering has a little increase under the same atmospheric condition, so $\tau_{sd,\lambda}$ has a slight increase. As for $\rho_{dd,\lambda}$, it is associated with atmospheric conditions but independent of the direction of solar incidence and observation, which represents the scattering albedo in hemisphere-hemisphere direction through the atmosphere. Therefore, it is independent of the change of solar incidence zenith angle.

3.3 Parameterization of atmospheric upward and downward radiative fluxes

Taking Landsat5 TM data as an example, the wavelength of its 6 visible-near infrared bands ranges from 0.4 to 2.5μm, as shown in Fig. 5, which is consistent with the spectral range of data used in the previous analysis on upward and downward radiation, therefore, the method described above can be directly used in atmospheric correction on TM data.

The corresponding value of TM bands can be obtained by the following equations through channel integral of $\tau_{ss,\lambda}$, $\tau_{sd,\lambda}$ and $\rho_{dd,\lambda}$:

$$\tau_i = \frac{\int \tau\ (\lambda)\phi_i(\lambda)\mathrm{d}\lambda}{\int \phi_i(\lambda)\mathrm{d}\lambda} \tag{21}$$

where, τ_i indicates the integral value by TM band response; $\phi_i(\lambda)$represents the spectral response value at each TM band.

The integral results of the 6 bands of Landsat5 TM data are analyzed by non-linear least square method to find the three atmospheric parameters τ_{ss}, τ_{sd} and ρ_{dd} with approximately the same form of regression equation, but with different scaling factor in different band. Finally, the fitting results of the three atmospheric parameters at each band are obtained, as shown in Table 2. The form of fitting equation is as follows:

$$\begin{aligned} \text{Fit\_Function} = P_1 * w^3 + P_2 * w^2 + P_3 * w + \quad &(a) \\ (P_4 * v + P_5)/(v + P_6) + \quad &(b) \\ P_7 * s^2 + P_8 * s \quad &(c) \end{aligned} \tag{22}$$

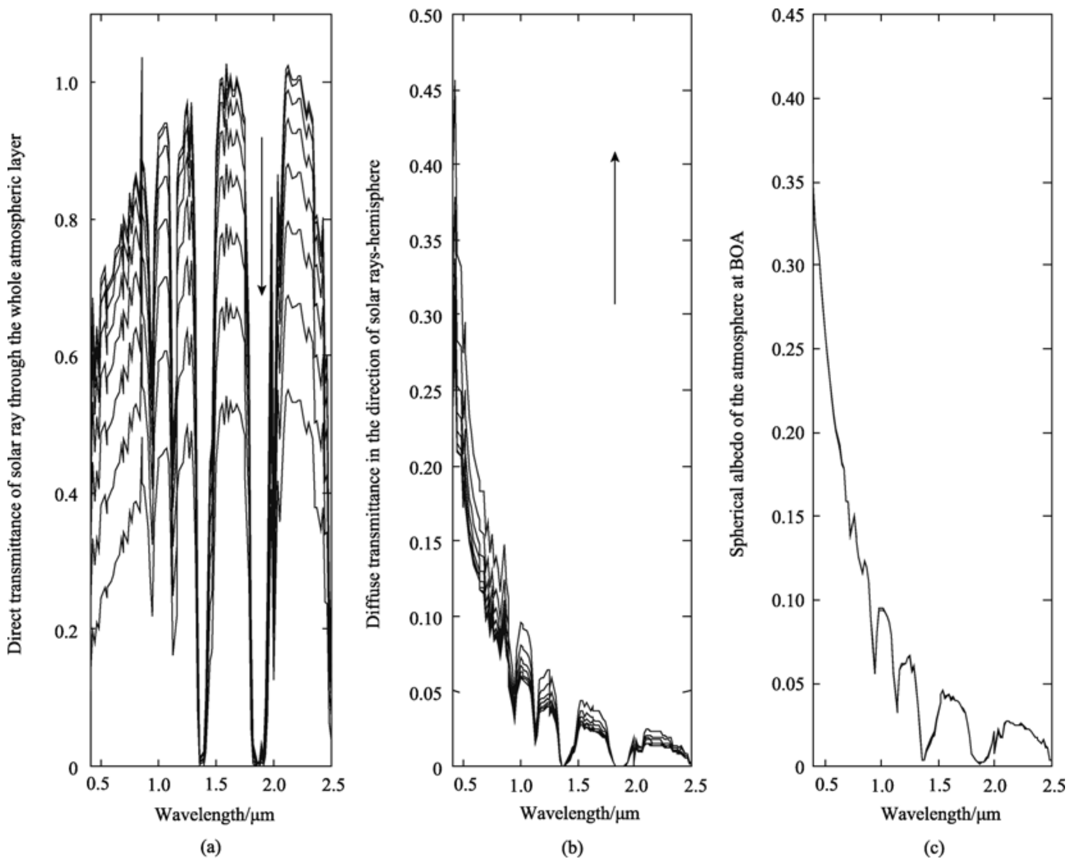

Fig. 4 Computing results of three atmospheric parameters in different solar incidence zenith angles
(a) Direct transmittance of solar ray through the whole atmospheric layer; (b) Diffuse transmittance in the direction of solar rays-hemisphere; (c) Spherical albedo of the atmosphere at BOA

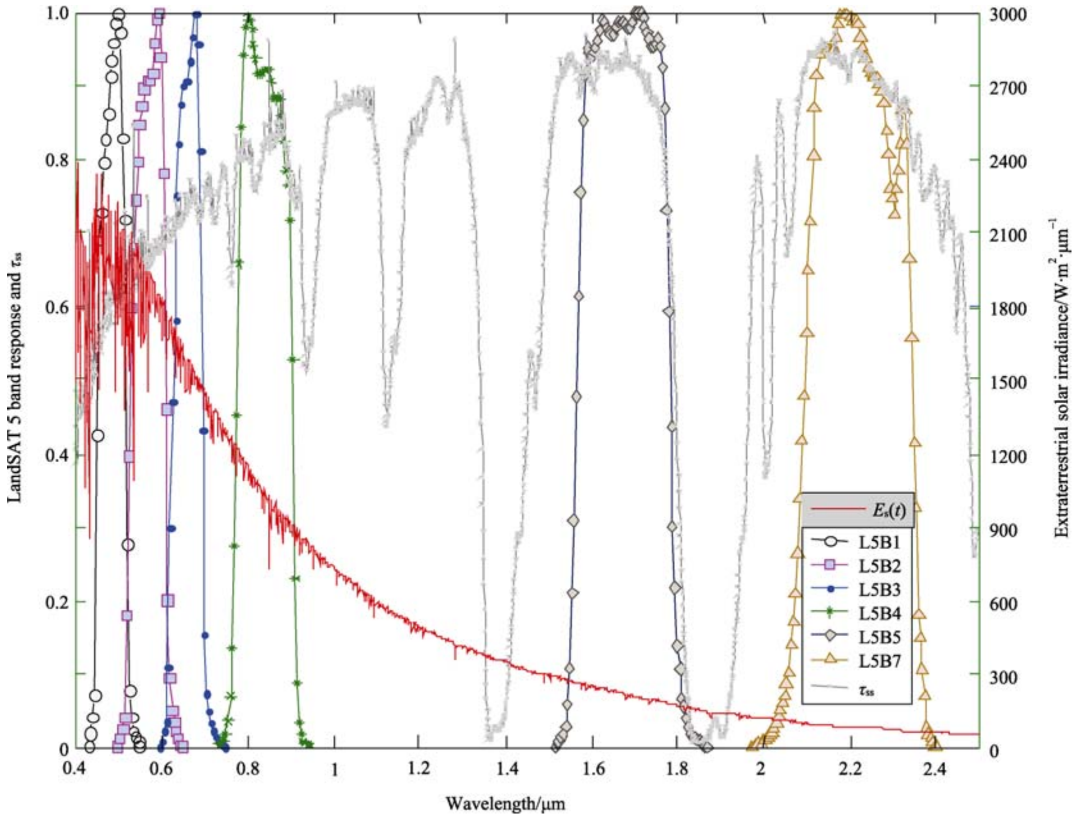

Fig. 5 Setting of Landsat 5 TM band, atmospheric transmittance and solar irradiance at TOA

Where P_1–P_8 are the equation coefficient items; w, v and s indicate the atmospheric water vapor content (g/cm^2), the horizontal meteorological visibility distance (km) and cosine value of solar incidence zenith angle ($\cos\theta_s$), respectively. Water vapor content is cubic polynomial function of the three atmospheric parameters, cosine of solar incidence zenith angle is quadratic polynomial function of them, and visibility distance is the first-order rational function of these parameters.

The following indicators are adopted to evaluate the accuracy of the fitting results (Zheng *et al*., 2004; He *et al*., 2005; Li *et al*., 2006):

(1) Root mean square error (RMSE) represents the global error distribution between the estimated and actual observed values of the model:

$$\mathrm{RMSE} = \sqrt{\frac{\sum_{i=1}^{n}(e_i - o_i)^2}{n}} \tag{23}$$

where e_i and o_i indicates estimated and observed values of the model, respectively.

(2) Mean bias indicates the errors between the estimated and total observed values of the model:

$$\text{Mean bias} = B = \frac{\sum_{i=1}^{n}(e_i - o_i)}{n} \tag{24}$$

(3) Precision indicates repeated estimation accuracy of the fitting model, that is, the standard deviation got by correcting the average deviation:

$$\text{Precision} = \sqrt{\frac{\sum_{i=1}^{n}(e_i - o_i - B)^2}{n-1}} \tag{25}$$

(4) Nash-Sutcliffe efficiency coefficient (E). It can express the commonly used decision coefficient R^2, which represents the consistence of the magnitude of global errors between estimated values and observed values of samples. In addition, it can fully express the consistence of the inner error distribution of the sample, which ranges from $-\infty$ to 1, the estimated value of the model coincide well with the observed value when E=1.0; The estimated precision is up to the average level of the observed value when E=0.0; the error of estimated value is large when E<0.0.

$$E = 1.0 - \frac{\sum_{i=1}^{n}|e_i - o_i|}{\sum_{i=1}^{n}|e_i - \bar{o}_i|} \tag{26}$$

Statistical analysis on the accuracy of fitting model is shown in Table 2, in which the accuracy of estimated value of the three atmospheric parameters has reached above 0.95; the maximum of RMSE and Precision are less than 1%; and mean deviation is 9 orders of magnitude smaller. Therefore, the regression fitting model is established with sufficient precision, able to accurately represent the atmospheric parameters value on conditions of different water vapor, visibility distance and solar incidence zenith angle.

Table 2 Fit coefficient of atmospheric parameters and evaluation results

Atmospheric parameters	Bands	Coefficient of w			Coefficient of v			Coefficient of s		Evaluation terms			
		P_1	P_2	P_3	P_4	P_5	P_6	P_7	P_8	E	RMSE	Mean bias	Precision
τ_{ss}	L5B1	-7.3020×10^{-5}	0.000902	−0.002000	0.283153	−10.136593	14.789664	−0.215574	0.924471	0.976668	0.007494	6.4740×10^{-12}	0.006188
	L5B2	1.6943×10^{-5}	−0.000195	0.000193	0.248674	−8.024970	10.849285	−0.249366	0.999136	0.979478	0.007597	1.1000×10^{-13}	0.006273
	L5B3	8.8840×10^{-5}	−0.000969	−0.001105	0.237893	−6.201035	7.923271	−0.272271	1.048734	0.979788	0.008429	-5.9850×10^{-12}	0.006960
	L5B4	1.0636×10^{-4}	−0.000624	−0.012719	0.242095	−4.023436	4.770824	−0.289582	1.098384	0.977383	0.009717	-1.1850×10^{-12}	0.008023
	L5B5	1.2605×10^{-4}	−0.000734	−0.017713	0.237681	−1.085536	1.124253	−0.263949	1.052227	0.988499	0.002578	2.3000×10^{-14}	0.002128
	L5B7	1.8587×10^{-4}	−0.002243	−0.007383	0.220485	−0.671325	0.635326	−0.261631	1.058064	0.987215	0.002570	-2.1700×10^{-13}	0.002122
τ_{sd}	L5B1	-6.5944×10^{-5}	0.000733	−0.000932	0.206946	21.899567	40.045200	0.183014	−0.409750	0.934833	0.002992	3.3259×10^{-11}	0.002412
	L5B2	-9.6375×10^{-5}	0.001142	−0.002230	0.157521	9.573606	19.666934	0.117804	−0.274629	0.958120	0.001750	3.2220×10^{-12}	0.001411
	L5B3	-1.2613×10^{-4}	0.001556	−0.004225	0.134619	5.953097	12.565856	0.100128	−0.230907	0.964484	0.001345	3.7000×10^{-13}	0.001084
	L5B4	-1.7901×10^{-4}	0.002297	−0.007375	0.099535	3.364813	7.942021	0.075218	−0.170346	0.964019	0.001161	4.6300×10^{-13}	0.000936
	L5B5	-1.5810×10^{-4}	0.001989	−0.005414	0.026680	0.764273	3.172737	0.020292	−0.046238	0.952023	0.000750	1.0000×10^{-15}	0.000605
	L5B7	-1.2722×10^{-4}	0.001587	−0.004247	0.015071	0.486015	2.376663	0.011527	−0.026883	0.951897	0.000582	-6.6000×10^{-14}	0.000469
ρ_{dd}	L5B1	-1.2526×10^{-4}	0.001448	−0.002485	0.132588	6.431340	10.446559	−0.001434	0.002890	0.990090	0.000960	-2.1000×10^{-14}	0.000784
	L5B2	-1.6153×10^{-4}	0.001932	−0.003977	0.080067	5.640540	9.371051	−0.001711	0.003311	0.982672	0.001045	1.0800×10^{-13}	0.000842
	L5B3	-2.0551×10^{-4}	0.002564	−0.007025	0.051947	4.769732	8.249795	−0.000659	0.001250	0.981714	0.001147	2.2800×10^{-13}	0.000924
	L5B4	-2.7906×10^{-4}	0.003577	−0.011035	0.028184	3.393486	6.895959	0.000224	−0.000571	0.975207	0.001395	-1.0000×10^{-15}	0.001125
	L5B5	-2.5608×10^{-4}	0.003223	−0.008834	0.003741	1.118045	3.871966	−0.000778	0.001295	0.959719	0.001173	-7.8000×10^{-14}	0.000946
	L5B7	-2.1060×10^{-4}	0.002627	−0.007135	0.000269	0.769926	3.011455	−0.001128	0.001866	0.955932	0.000944	9.1000×10^{-14}	0.000761

3.4 Estimation of the atmospheric upward and downward radiation fluxes in Landsat5 TM

3.4.1 Analysis of ratio $\dfrac{E^{+}(b)}{E^{-}(b)}$

With combination of Landsat 5 band settings, the relationship of Q value with water vapor content, visibility distance, solar incidence zenith angle and surface reflectance is analyzed according to the regression model of the three atmospheric parameters obtained above, as shown in Fig.6. Under the conditions of the same surface albedo but different water vapor content, the change of Q value is not significant. However, the ratio of Q increases approximately linearly with the wavelength. Its reason is that the effect of atmospheric transmission on radiation mainly concentrates at the elevation below 10 km in the atmosphere. It can be seen from Fig.2, the two atmospheric parameters ($\tau_{sd,\lambda}$ and $\rho_{dd,\lambda}$) related to $E^{-}(b)$ decrease with the increase of water vapor content, and significantly decrease with wavelength increasing, which leads to the $E^{-}(b)$ decrease. Under the assumption of Lambertian surface, characteristic parameters of surface reflectance $\overline{r_{sd}}$ and $\overline{r_{dd}}$ involved in $E^{+}(b)$ remain constant, but the two should have slightly increased in theory. Thus, the value of Q is always greater than 1 and tends to increase with the wavelength.

The values of Q corresponding to L5B1-L5B4 band are all less than 4, while that corresponding to L5B1 and L5B7 band reach about 10—16.

It can be seen from the right part, Q increases exponentially with the surface albedo, and the value ranges up to about 0.1—25 times. There are large differences in the amplitude of increase in different bands, where L5B1— L5B3 band has slight increase, while the other three bands have large increase reaching around 26 times.

It can be seen from Fig.7 that Q also increases with the wavelength, and the value at L5B7 band is 15 times higher than

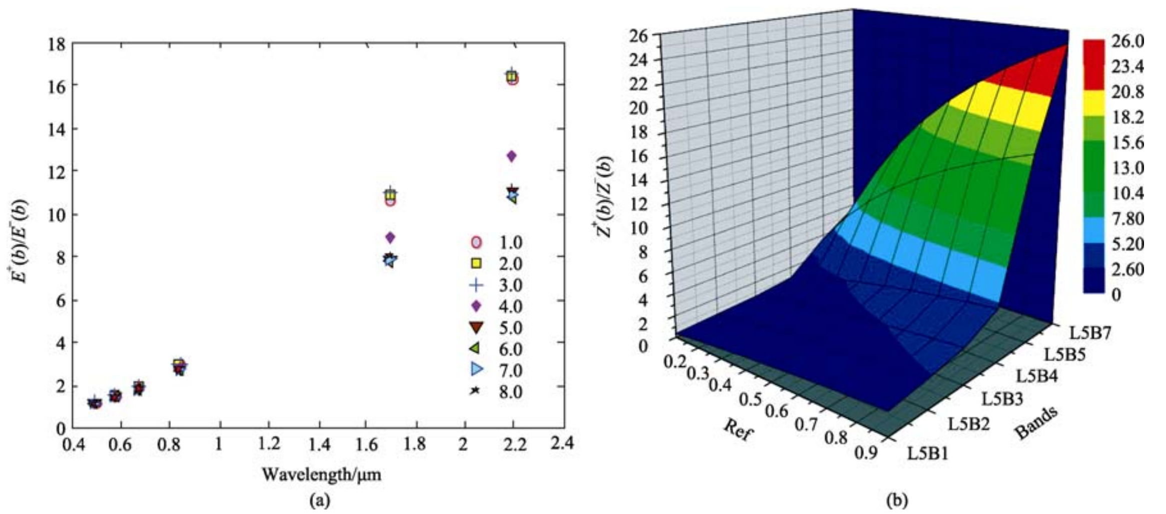

Fig. 6 Relationship between Q and water vapor (a) and reflectance (b)
(a) ref=0.4, w=1.0—8.0g/cm^2; (b) ref=0.1—0.9, w=1.0g/cm^2

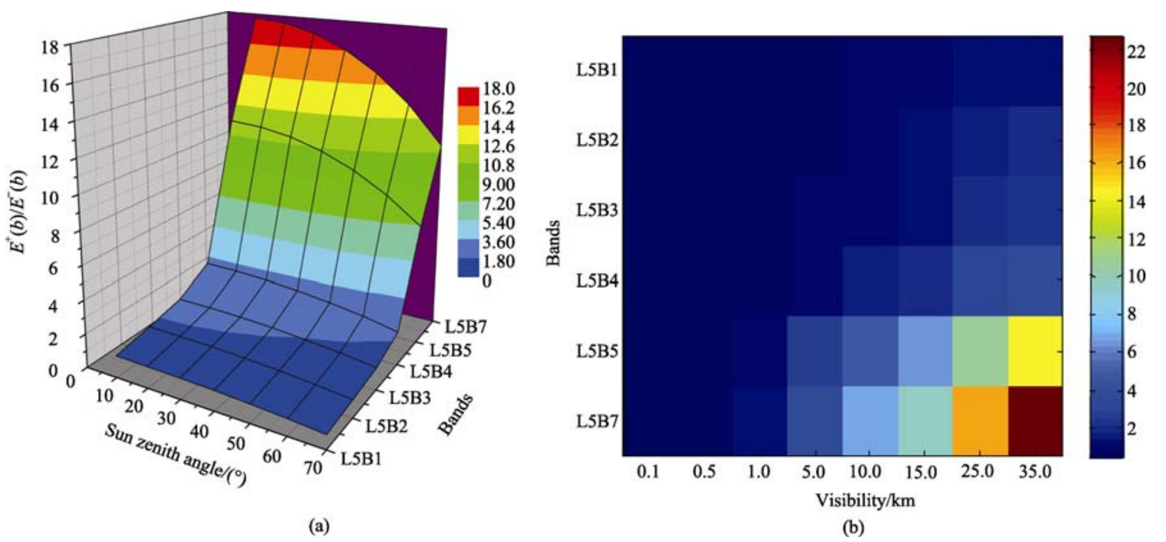

Fig. 7 Relationship between Q with solar zenith angle and visibility distance
(a) Different solar incidence zenith angle; (b) Different visibility distance

that at L5B1 band; but it decreases with the increase of solar incidence zenith angle; the value is on negative exponential decline at 0—70° of solar incidence zenith angle at each band, with the largest attenuation as half of that at 0°. Under the conditions of different visibility distance, Q increases in form of quadratic polynomial function of the band sequence and visibility distance, and the amplitude of increase is slightly larger than the former, with maximum reaching 22.

3.4.2 Estimation of the atmospheric upward/downward radiation fluxes in TM narrow band

The selected image of Landsat 5 TM, overpass Beijing in June 2nd, 2009, path/row: 123/32, was used in the study. The area is located in Changping District of Beijing, mainly covered with winter-wheat, bare soil and buildings. The surface of the experimental area is flat, with the altitude of 52 m. Based on the data observed by the weather station, the estimated water vapor content is 2.82 g/cm^2; visibility distance is 22 km; solar incidence zenith angle in the satellite transmitting is 33.2°. Other atmospheric parameters in Eq. (11) can also be calculated through running MODTRAN 4 for three times with reference to the computing method of $\tau_{ss,\lambda}$, $\tau_{sd,\lambda}$ and $\rho_{dd,\lambda}$. And the corrected surface reflectance can be obtained by means of the calibrated TM data, as shown in Fig.8.

Through the computing formula of $E^+(b)$, $E^-(b)$ and Q, the solar irradiance data with the resolution of one wave number are used to calculate the atmospheric upward and downward radiation fluxes of the 6 bands of TM and the ratio between them, as shown in Fig.9 and Fig.10.

It can be seen from the results above: (1) $E^+(b)$ is significantly lower than $E^-(b)$ at L5B1 band under vegetation coverage; $E^-(b)$ is near 430 W m^{-2} μm^{-1}, but $E^+(b)$ is only about 45 W m^{-2} μm^{-1} which is nearly 10 times lower than the former. It is consistent with the results obtained above. In the non-vegetation covered area, $E^+(b)$ is about 100 W m^{-2} μm^{-1}, but $E^-(b)$ is still around 450 W m^{-2} μm^{-1}. The results show that there are large differences in $E^+(b)$ for the coverage of vegetation and for the bare soil at L5B1 band, which are greatly affected

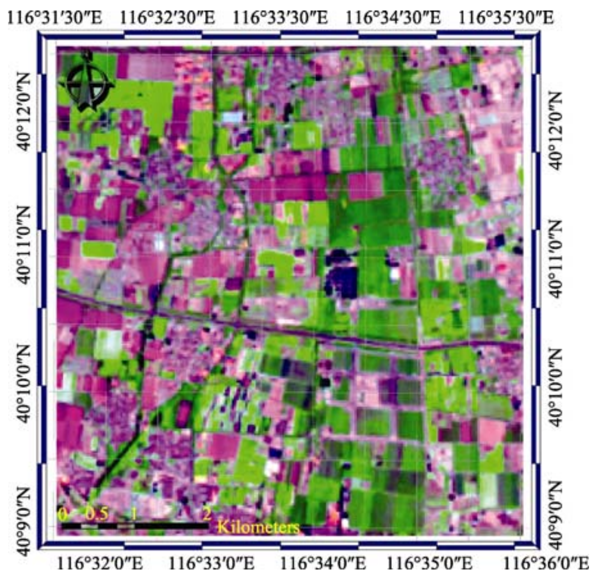

Fig. 8 Reflectance of Landsat 5 TM (R:7, G:4, B:3)

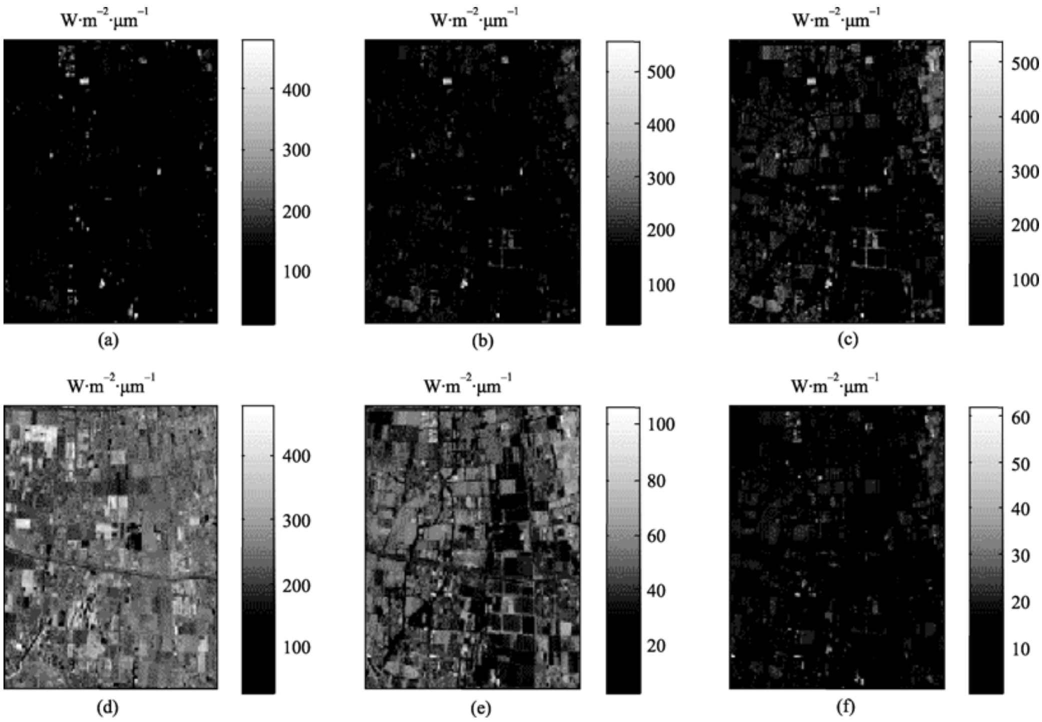

Fig. 9 Total diffuse upward flux for six bands of Landsat 5 TM
(a) L5B1; (b) L5B2; (c) L5B3; (d) L5B4; (e) L5B5; (f) L5B7

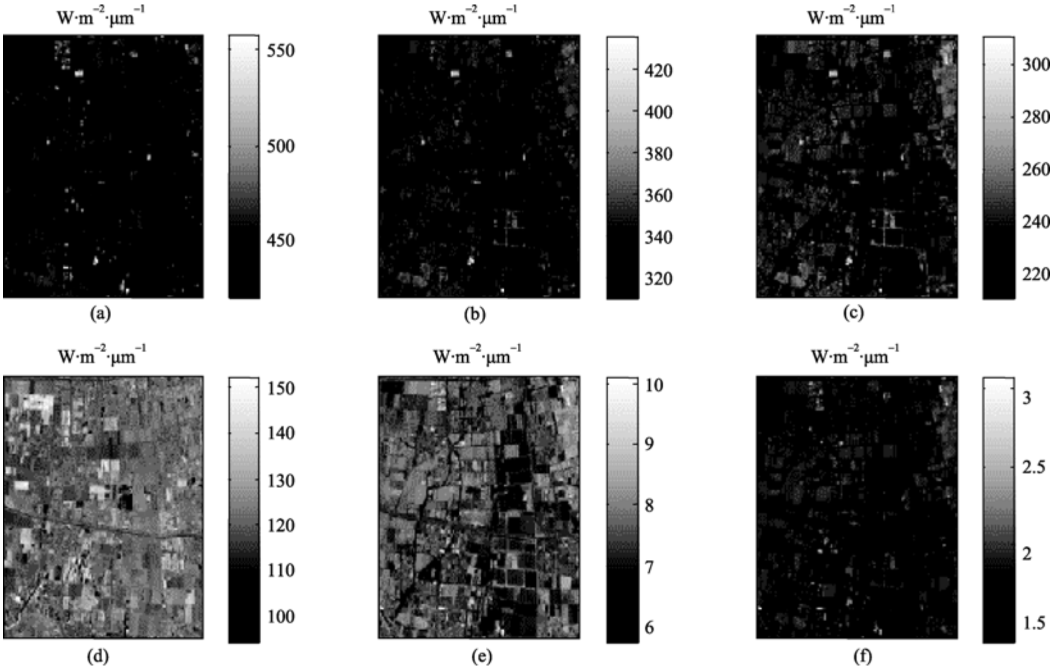

Fig. 10 Total diffuse downward flux for six bands of Landsat 5 TM
(a) L5B1; (b) L5B2; (c) L5B3; (d) L5B4; (e) L5B5; (f) L5B7

by the reflection characteristics of surface. However, $E^{-}(b)$ is nearly the same in the two different kinds of surface features and less correlated with surface condition. (2) $E^{+}(b)$ for bare soil is about 2—3 times larger than that for vegetation coverage; $E^{+}(b)$ for vegetation coverage is around 80 W m^{-2} μm^{-1}; but $E^{-}(b)$ is little correlated with surface features, for example, it is just 20 W m^{-2} μm^{-1} lower for the coverage of vegetation than for bare soil. (3) The value of $E^{+}(b)$ and $E^{-}(b)$ changes according to similar laws at L5B3and L5B2 bands, and $E^{+}(b)$ reaches its maximum in bare soil as about 200 W m^{-2} μm^{-1}; $E^{-}(b)$ for the coverage of vegetation is just 30 W m^{-2} μm^{-1} lower than that for bare soil. (4) At L5B4 band, $E^{+}(b)$ for the coverage of vegetation is 50 W m^{-2} μm^{-1} higher than that for bare soil, and the maximum value reaches around 250 W m^{-2} μm^{-1}; $E^{-}(b)$ is nearly the same in the two types of area, around 110 W m^{-2} μm^{-1}.(5) Both $E^{+}(b)$ and $E^{-}(b)$ at L5B5 band are significantly lower than those at the four bands above, with the largest amplitude of decrease 10 times more than before; $E^{+}(b)$ is about 5 times higher than $E^{-}(b)$, but both of them are less affected by surface features, and $E^{+}(b)$ is about 40 W m^{-2} μm^{-1}. (6) At L5B7 band, $E^{+}(b)$ and $E^{-}(b)$ are much smaller, $E^{-}(b)$ for the coverage of vegetation is nearly the same with that for the bare soil, as around 2 W m^{-2} μm^{-1}; while $E^{+}(b)$ for the coverage of vegetation is about 1/3 of that for bare soil, as around 7 W m^{-2} μm^{-1}. The solar irradiance at TOA gradually decreases at the wavelength longer than 0.4 μm, the amplitude of decrease is up to 40 times that at the wavelength of 2.5μm, as shown in Fig.5. Thus, $E^{+}(b)$ and $E^{-}(b)$ tend to decrease from L5B1to L5B7. In general, $E^{+}(b)$ in the first three bands are lower than $E^{-}(b)$, but gradually become higher than $E^{-}(b)$ from the fourth band.

3.5 Discussion

The four-stream approximated atmospheric radiative transfer analytical model described in the paper has been successfully applied in the atmospheric correction of multi-spectral and hyperspectral remote sensing data. To solve the atmospheric parameters independent of surface features in the model, the assumption of Lambertian surface was introduced. The models were solved with equations established simultaneously under the conditions of different surface albedo. By comparing the total radiation at entrance pupil calculated by the analytical model with four-stream approximation and the original MODTRAN4, that was, the output results of MODTRAN 4 model were considered as the true value, the relative error between the obtained result in the paper and that in MODTRAN4 model was computed. The results showed that the relative errors were less than 0.5% for all bands, as shown in Fig.11. Meanwhile, the values of the three parameters, $\tau_{ss,\lambda}$, $\tau_{sd,\lambda}$ and $\rho_{dd,\lambda}$, were compared with the results computed by Verhoef *et al.* (2003), which showed full consistence in the parametric value range and precision.

The simplified analytical model of four-stream approximated atmospheric radiative transfer presented in the paper was applied in the remote sensing imaging simulation. Under the assumption of Lambertian surface, atmospheric radiation fluxes were analyzed, and the parameterization and computation of the atmospheric upward and downward radiation of Landsat 5 TM were conducted. Thus Eq. (6) could be transformed into Eq. (11), and Eq. (7)—Eq.(9) were transformed into Eq. (10), which implied that the scale of surface neighboring effect was the same with the spatial scale of ground object, that was, the

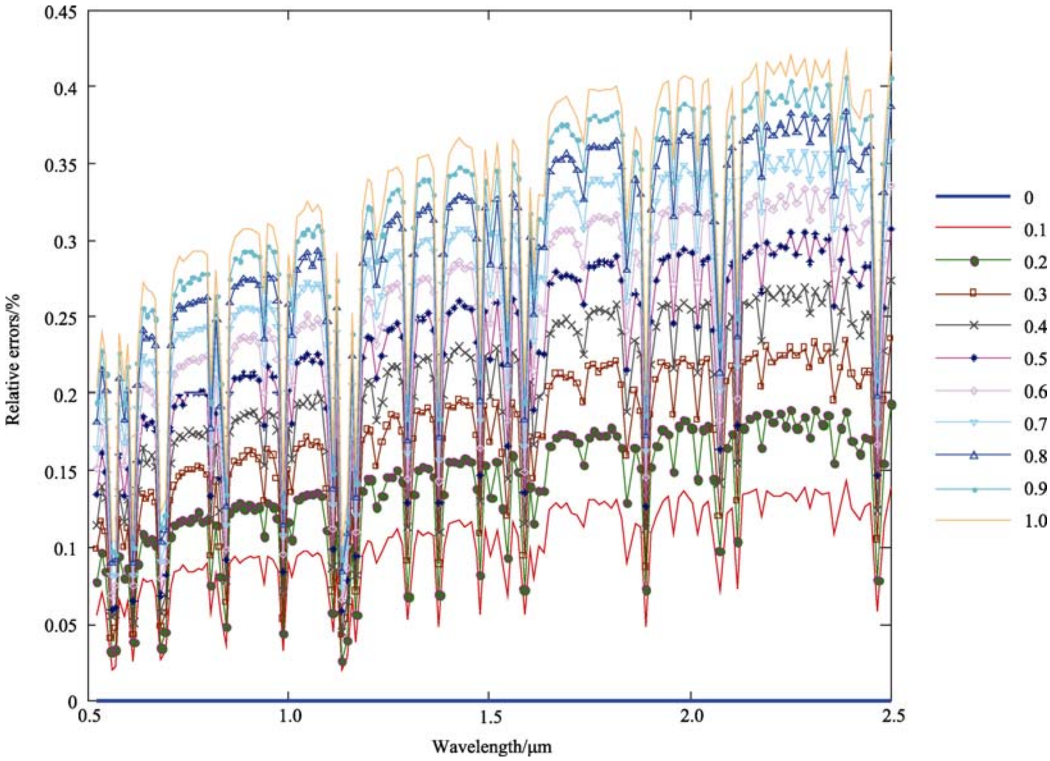

Fig. 11 Errors analysis of the analytical model of atmospheric radiative transfer

neighboring objects corresponding to the two items $\overline{r_{sd}}$ and $\overline{r_{dd}}$ in Eq. (3) were assumed to be the Lambertian with the same reflectance of the ground object. The result of the processing above was that, the pixel was considered as homogeneous infinite Lambert surface while computing the atmospheric upward and downward radiation of each pixel of Landsat 5 TM image. In this case, the role of neighboring effect reached their maximum, with the same resolution with the pixel. Of course, this was a typical case for Eq.(3), for example, Eq. (10)— Eq. (11) were reasonable in a relatively homogeneous large area of water bodies and desert surface. If considering the neighboring effect, after computing the three parameters $\tau_{ss,\lambda}$, $\tau_{sd,\lambda}$ and $\rho_{dd,\lambda}$ under the assumption of Lambertian surface, $\overline{r_{sd}}$ and $\overline{r_{dd}}$ should be calculated by the direct method of radiative transfer model for the different surface features or by the indirect method of atmospheric point spread function(Hu *et al.*, 1996; Niu *et al.*, 1997; Xiao *et al.*, 2005). Preliminary estimation showed that the contribution of neighboring effect caused by $\overline{r_{sd}}$ and $\overline{r_{dd}}$ was about 5% for Landsat5 TM data used in the paper under the condition of horizontal meteorological visibility distance of 22km. Therefore, the atmospheric upward and downward radiation of one pixel could be compared only in the pixel scale, and the condition that different features with different scale and magnitude of the neighboring effect should be considered in the precision calculation. That is to say, neighboring effect caused by $\overline{r_{sd}}$ and $\overline{r_{dd}}$ will make $E^{+}(b)$ vague just as performing low-pass filter in different degrees, and further affect $E^{-}(b)$. One of the purposes of this paper is to apply atmospheric radiative transfer analytical model in the simulation of remote sensing image and the evaluation of the response properties of sensor under ideal conditions. In our subsequent study, ray tracing method will be used to calculate the neighboring effect approximately, obtain the PSF value for each pixel and spatial extent, and compute atmospheric upward and downward radiation fluxes in the actual situation.

4 CONCLUSIONS

According to the four-stream radiative transfer theory, the numeral model of visible-near infrared band atmospheric radiative transfer was developed with consideration of the contribution of atmospheric upward and downward diffuse reflectance at entrance-pupil. From MODTRAN 4 model, the atmospheric parameters corresponding to the two items referred above have been calculated, and the three atmospheric parameters of transmittance of direct sun light through the whole atmospheric layer $\tau_{ss,\lambda}$, the diffuse transmittance in the direction of solar rays-hemisphere $\tau_{sd,\lambda}$ and atmospheric spherical albedo at BOA $\rho_{dd,\lambda}$ have been obtained. It was determined that the key factors affecting the three atmospheric parameters were water vapor content, meteorological visibility distance and solar incidence zenith angle through analysis. The conclusions that the value of 60% water vapor content was about 1.0, ranging from 0.1 to 8.0 g/cm^2; visibility distance was within 0.1—35 km; solar incidence zenith angle ranged from 0° to 70° were drawn from TIGR atmospheric profiles database. According to the parameters' value range referred above and different combination of them, the sensibility of the three atmospheric parameters has been analyzed, and results are shown as follows: (1) There is not significant change of the three atmospheric parameters with different water vapor content, and that decrease is only about 5% with water vapor content increasing. (2) The greatest change of the three atmospheric parameters caused by different aerosol visibility ranges up to about 10 times. $\tau_{ss,\lambda}$ and $\tau_{sd,\lambda}$ increase with the visibility distance, but $\rho_{dd,\lambda}$ is opposite to the situation. (3) $\tau_{ss,\lambda}$ gradually decreases with the solar incidence zenith angle increasing, and the change range can reach about 10times; on the contrary $\tau_{sd,\lambda}$ is with small increase; $\rho_{dd,\lambda}$ is independent of solar incidence zenith angle and keeps constant.

Besides, it can be found that the three atmospheric parameters have the same parameterized form after performing regression analysis on them, where water vapor content was cubic polynomial of the three atmospheric parameters, and the cosine of solar incidence zenith angle was quadratic polynomial of them, visibility distance was a first-order rational function of these parameters. The model estimation precision (E) of the three atmospheric parameters is more than 95%, and the biggest RMSE and Precision are all smaller than 1%, which demonstrates that the parametric model has the greatest precision. In addition, through computing atmospheric upward and downward diffuse radiation of the Landsat5 TM 6 narrow bands, it is concluded that the change of the Q value is not obvious under the different conditions of water vapor content, but the value of Q increased approximately linear with the wavelength, in contrast with the situation of atmospheric irradiance decreasing at TOA; the value of Q tends to increase exponentially with atmospheric water vapor content, meteorological visible distance and solar incidence zenith angle, ranging from 0.1 to 25 times, but there are large differences at different bands in changing extent.

Through analyzing atmospheric upward and downward diffuse radiation of TM bands, it can be found that $E^{-}(b)$ is approximately the same either for vegetation coverage of vegetation or for bare soil, but it decreases with the band sequence; whereas $E^{+}(b)$ under coverage of vegetation is 2—4 times larger than that in bare soil besides L5B4 and L5B5 with the similar value of $E^{+}(b)$.

In the paper, the upward and downward radiations were calculated based on the assumption of Lambertian surface. The values were obtained under the ideal diffuse reflection condition, which has certain differences from the actual situation. In addition, the method is only suitable for flat areas as the factors affecting the radiation of topography and elevation were neglected. The problems above will be the focus of our further studies.

REFERENCES

Abduwasit G, Qin Q M and Zhu L J. 2004. 6S model based atmospheric correction of visible and near infrared data and sensitivity analysis. *Acta Scientiarum Naturalium Universitatis Pekinensis*, **40**(4): 116—816

Aires F, Alain C, Noëlle A S and Rossow W B. 2002. A regularized neural net approach for retrieval of atmospheric and surface temperatures with the IASI instrument. *Journal of Applied Meteorology*, **41**(2): 144—159

Berk A, Anderson G P, Acharya P K, Chetwynd J H, Bernstein L S, Shettle E P, Matthew M W and Adler-Golde S M. 2000. MODTRAN4 Users Manual, Air Force Research Laboratory, Space Vehicles Directorate, Air Force Materiel Command, Anscom AFB, MA 01731—3010.

Ellicott E, Vermote E, Petitcolin F and Hook S J. 2009. Validation of a new parametric model for atmospheric correction of thermal infrared data. *IEEE Transactions Geoscience and Remote Sensing*, **47**(1): 295—311

Ghulam Abduwasit, Qin Q M and Zhu L J. 2004. 6S Model based atmospheric correction of visible and near infrared data and sensitivity analysis *Acta Scientiarum Naturalium Universitatis Pekinensis*, **4**(40): 116—816

Gastellu-Etchegorry J P, Martin E and Gascon F. 2004. DART: A 3D model for simulating satellite images and studying surface radiation budget. *International Journal of Remote Sensing*, **25**: 73—96

He L M, Yan G J, Wang Q and Li X W. 2005. Models and its analysis about the atmospheric correction of optical remote sensing imagery. *Geo-Information Science*, **7**(4): 32—38

Hu B X, Li X W, Zhu C G and Strahler A H. 1996. Deriving the anisotropic atmospheric pointspread function of off-nadir remote sensing. *Journal of Image and Graphics*, (1): 19—29

Kaufman Y J and Sendra C. 1988. Algorithm for automatic atmospheric corrections to visible and near-IR satellite imagery. *International Journal of Remote Sensing*, **9**(8): 1357—1381

Liang S L, Fang H L and Chen M. 2001. Atmospheric correction of landsat ETM+ land surface imagery—Part Ⅰ: methods. *IEEE Trans Geosci Remote Sensing*, **39**: 2490—2498

Liang S L and Fang H L. 2004. An improved atmospheric correction algorithm for hyperspectral remotely sensed imagery. *IEEE Trans Geosci Remote Sensing*, **1**(2): 112—117

Li Q L, Xue Y Q, Wang J Y and Bai Z Q. 2006. Atmospheric correction of PHI hyperspectral imagery. *Journal of Infrared and Millimeter Waves*, **25**(4): 613—913

Nie A X, Zhang L T and Chen Z A. 2007. A practical atmospheric correction method and its application in the hyperion image. *Journal of East China Institute of Technology*, **30**(2): 157—160

Niu Z, Zhu C G and Wang C Y. 1997. Analysis of atmospheric cross radiation in a slant viewing angle. *Journal of Remote Sensing*, **1**(2): 88—93

Qin W and Gerstl S A. 2000. 3-D Scene modeling of semi-desert vegetation cover and its radiation regime. *Remote Sensing of Environment*, **74**: 145—162

Vermote E F, Saleous N Z and Justice C O. 2002. Atmospheric correction of the MODIS data in the visible to middle infrared: first results. *Remote Sensing of Environment*, **83**(1): 97—111

Verhoef W. 1984. Light scattering by leaf layers with application to canopy reflectance modeling: the sail model. *Remote Sensing of Environment*, **16**: 125—141

Verhoef W and Bach H. 2003. Simulation of hyperspectral and directional radiance images using coupled biophysical and atmospheric radiative transfer models. *Remote Sensing of Environment*, **87**: 23—41

Xiao Q, Liu Q H, Li X W, Chen L F and Liu Q. 2005. Analysis and correction of atmospheric cross radiation for high geometric resolution airborne remote sensing data. *Journal of Remote Sensing*, **9**(6): 625—633

Yang G J, Liu Q H, Liu Q, Xiao Q, Gu X F and Huang W J. 2009. Mid-infrared atmosphere radiation transfer analytic model and remote sensing images simulation. *Spectroscopy and Spectral Analysis*, **29**(3): 629—633

Yang G J, Liu Q H, Liu Q, Xiao Q and Gu X F. 2008. Adjacency effect analysis in imaging simulation of high-resolution mid-infrared (3—5μm) remote sensing. *Journal of Infrared and Millimeter Waves*, **27**(3): 1—8

Yang G J, Liu Q H, Huang H G, Liu Q and Gu X F. 2007. Methods for simulating infrared remote sensing imagines based on scene models. *Journal of Infrared and Millimeter Waves*, **26**(1): 1—7

Zheng W and Zeng Z Y. 2004. A review on methods of atmospheric correction for remote sensing images. *Remote Sensing Information*, (4): 66—96

可见光-近红外波段大气上行与下行辐射分量参数化方法

杨贵军[1,2], 高中灵[1,3], 黄文江[1], 刘 强[1], 王纪华[1], 张明月[1]

1. 国家农业信息化工程技术研究中心, 北京 100097;
2. 遥感科学国家重点实验室, 中国科学院 遥感应用研究所, 北京 100101;
3. 北京师范大学 地理学与遥感科学学院, 北京 100875

摘 要: 可见光-近红外波段大气上行、下行辐射是辐射传输建模、成像模拟及大气校正关键的输入参数, 根据四流辐射传输理论给出了与二者相关大气参量的数值模型及计算方法, 针对 Landsat 5 TM 6 个波段建立了大气参量与水汽含量、能见度距离和太阳入射天顶角间的参数化模型, 在此基础上对各参量间敏感性进行了分析, 结果表明参数化模型具备较高精度。同时, 计算了各波段大气上行、下行漫射辐射值, 对二者在植被和裸土覆盖条件下的差异进行了定量分析。

关键词: 大气上行、下行辐射, 辐射传输, 大气校正, 参数化模型

中图分类号: TP722.5/P407 **文献标识码:** A

引用格式: 杨贵军, 高中灵, 黄文江, 刘 强, 王纪华, 张明月. 2010.可见光-近红外波段大气上行与下行辐射分量参数化方法. 遥感学报, **14**(4): 637—662
Yang G J, Gao Z L, Huang W J, Liu Q, Wang J H and Zhang M Y. 2010. Parameterization methods of atmospheric upward and downward radiation fluxes in visible and near-infrared bands. *Journal of Remote Sensing*. **14**(4): 637—662

1 引 言

大气层对太阳辐射的影响主要表现在散射与吸收。由于大气的存在, 太阳辐射因大气中水分分子以及气溶胶粒子的吸收和散射减弱, 同时部分散射和太阳辐射的下行辐射进入到传感器, 使大气背景和地表信息混叠在一起, 限制了遥感数据的定量化应用。关于如何建立有效的大气辐射传输模型, 实现遥感数据的精确大气校正一直是众多研究者关注的热点问题。经过大量大气和遥感科学工作者多年的努力, 已经成功地开发并建立了宽、窄光谱带和逐个光谱线计算的大气辐射传输模型, 这些传输模型包括多种观测方式, 适用于非常宽的电磁波谱范围及多种可变气象要素。目前比较通用的大气辐射传输模型有 6S、LOWTRAN、MODTRAN 和 FASCODE 等, 但这些模型需要提供大量详细的大气参数, 且未直接给出各大气上行、下行辐射分量结果。在上述模型基础上已经有相应的商业大气校正工具, 例如 ATCOR、FLAASH 和 ACORN 等, 但同样需要提供详细的输入参数。目前, 大多数研究者根据不同传感器载荷和特定需要, 设计了不同的大气辐射传输简化计算模型, 例如 Liang 等(2001, 2004)、吾拉木等(2004)、聂爱秀等(2007)将传感器入瞳辐射分解为两项(Kaufman & Sendra, 1988; Vermote 等, 2002): 大气程辐射、太阳直射辐射经地面与大气下界(bottom of atmosphere, BOA)作用后的多次散射辐射。通过改变地表反射率条件和传感器高度, 利用 MODTRAN 模型间接计算出设定大气状况、太阳-地物目标-传感器间观测几何及传感器通道范围条件下的程辐射项(L_0)、太阳下行总辐射(F_d)、大气的半球反照率(S)及地物目标与传感器间透过率(T_μ), 并建立相应查找表。以上方法均未考虑大气上行、下行漫射辐射对

收稿日期: 2009-07-30; 修订日期: 2009-12-15
基金项目: 国家自然科学基金(编号: 40901173), 北京市自然科学基金(编号: 4102021), 中国科学院遥感应用研究所遥感科学国家重点实验室开放基金(编号: 2009KFJJ020), 农业公益性行业科研专项(编号: 200803037)。
第一作者简介: 杨贵军(1976—), 国家农业信息化工程技术研究中心助理研究员, 主要从事定量遥感应用、图像分析处理和 3S 集成开发及资源遥感监测等相关技术研究。E-mail: guijun.yang@163.com。

传感器入瞳辐射的贡献；实际来自地表的辐射中包含了地物直接反射的太阳直射辐射外，还有经过邻近地物散射后的大气上行漫射辐射和地物目标反射的大气下行漫射辐射。不考虑后两者辐射贡献时进行大气校正会存在一定程度的矫正不足，即计算出的大气参数对应的大气条件要优于真实大气状况。此外，在地表辐射传输建模过程中，更多学者将地-气辐射传输耦合过程统一考虑，例如 RGM、DART 等三维辐射传输模型中(Qin & Gerstl, 2000; Gastellu-Etchegorry 等, 2004)，需要提供给定波段范围内大气上行、下行辐射值。所以，关于定量化计算大气上行、下行辐射分量是有效解决上述问题的关键。

2　大气辐射传输数值模型建立

大气辐射传输参数化建模的基本思路是：(1) 建立包含大气上行、下行辐射分量的大气辐射传输数值模型，能够将二者从传感器入瞳辐射中分离开来；(2) 利用 6S、MODTRAN 等模型(Kaufman & Sendra, 1988; Berk 等, 2000; Vermote 等, 2002)对建立的数值模型进行求解，求出可见光-近红外宽波段(0.4—2.5μm)内大气上行、下行辐射分量；(3) 根据可见光—近红外波段影响大气辐射传输的关键大气因子，对二者进行多元非线性回归分析，建立参数化模型。

在可见光-近红外波段范围内，传感器接收的辐射主要来自反射的太阳辐射，其与大气相互作用的四流近似如图 1 所示。为了使四流近似表达公式命名规范，定义以下符号变量：ρ表示与大气相关的散射过程；τ表示大气直射或(前向)散射透过率；r 表示与地表相关的方向性反射；下标 s 表示太阳入射方向；下标 d 表示上行或下行半球漫射方向；下标 o 表示传感器观测方向；b,t 分别代表大气底层和大气顶层高度。

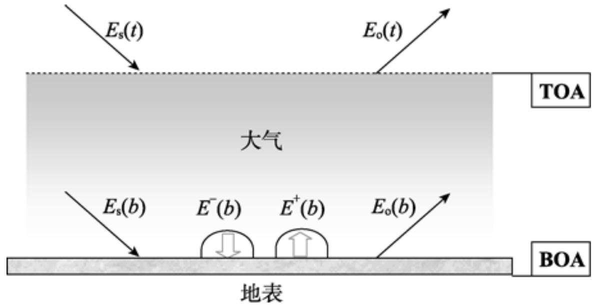

图 1　大气辐射传输过程示意图

根据四流大气辐射传输理论，与大气辐射传输相关的通量满足以下方程：

$$E_s(b) = \tau_{ss} E_s(t) \tag{1}$$

$$E^-(b) = \tau_{sd} E_s(t) + \rho_{dd} E^+(b) \tag{2}$$

$$E^+(b) = \overline{r_{sd}} E_s(b) + \overline{r_{dd}} E^-(b) \tag{3}$$

$$E_o(b) = r_{so} E_s(b) + r_{do} E^-(b) \tag{4}$$

$$E_o(t) = \rho_{so} E_s(t) + \tau_{do} E^+(b) + \tau_{oo} E_o(b) \tag{5}$$

式中，$E_s(t)$为大气层顶(top of atmosphere, TOA)入射太阳辐射通量，$E_s(b)$是到达大气层底(bottom of atmosphere, BOA)太阳直射辐射通量，$E^+(b)$和 $E^-(b)$分别为天空光上行、下行漫射辐射，$E_o(b)$是传感器观测方向 BOA 处地表总辐射，$E_o(t)$为传感器观测方向 TOA 处接收到的总辐射。τ_{ss} 为沿太阳方向直射透过率，τ_{sd} 为太阳光线方向-半球方向漫射透过率，τ_{do} 是半球至传感器观测方向漫射透过率，τ_{oo} 为地表至传感器观测方向直射透过率。ρ_{dd} 为 BOA 处大气球面散射反照率，ρ_{so} 为 TOA 处大气双向反射率。$\overline{r_{sd}}$ 和 $\overline{r_{dd}}$ 分别为关于地表太阳直射、大气下行散射的环境平均漫反射系数，r_{so} 为地表双向反射率，r_{do} 为半球-传感器观测方向反射率。

通过上述方程联立求解，可得大气层顶表观反射率 $r_{p,\lambda}$：

$$\begin{aligned}
r_{p,\lambda} = {} & \rho_{so,\lambda} + && \text{(a)} \\
& \tau_{do,\lambda} \frac{(\overline{r_{sd,\lambda}}\tau_{ss,\lambda} + \overline{r_{dd,\lambda}}\tau_{sd,\lambda})}{1-\overline{r_{dd,\lambda}}\rho_{dd,\lambda}} + && \text{(b)} \\
& \tau_{oo,\lambda} r_{do,\lambda} \frac{(\tau_{sd,\lambda} + \tau_{ss,\lambda}\overline{r_{sd,\lambda}}\rho_{dd,\lambda})}{1-\overline{r_{dd,\lambda}}\rho_{dd,\lambda}} + && \text{(c)} \\
& \tau_{oo,\lambda} r_{so,\lambda} \tau_{ss,\lambda} && \text{(d)}
\end{aligned} \tag{6}$$

其中(a)、(b)、(c)及(d)分别表示 TOA 处单次散射辐射、大气上行漫射辐射、大气下行漫射辐射及地表反射太阳直射辐射对传感器入瞳处总辐射贡献。

同样将方程(1)—(3)联立，可以得出：

$$E^+(b) = \frac{(\overline{r_{sd}}\tau_{ss} + \overline{r_{dd}}\tau_{sd})}{1-\overline{r_{dd}}\rho_{dd}} E_s(t) \tag{7}$$

$$E^-(b) = \frac{(\tau_{sd} + \tau_{ss}\overline{r_{sd}}\rho_{dd})}{1-\overline{r_{dd}}\rho_{dd}} E_s(t) \tag{8}$$

进而得到：

$$Q = \frac{E^+(b)}{E^-(b)} = \frac{(\overline{r_{sd}}\tau_{ss} + \overline{r_{dd}}\tau_{sd})}{(\tau_{sd} + \tau_{ss}\overline{r_{sd}}\rho_{dd})} \tag{9}$$

可以看出在可见光-近红外波段范围内大气下行和上行漫射辐射同时受太阳入射角度、大气状况和地表条件共同影响，与传感器观测角度无关。为了求解出二者及比值，必须事先得到公式中的大气

参数及环境特性参数。可假设地表为均一朗伯体，定义波长 λ 处地表反照率为常量 α_λ (地表反照率指地表对入射的太阳辐射的反射通量与入射的太阳辐射通量的比值)，并代替公式中与地表反射相关变量，可得到:

$$Q=\frac{E^{+}(b)}{E^{-}(b)}=\frac{\alpha_\lambda(\tau_{\text{ss},\lambda}+\tau_{\text{sd},\lambda})}{(\tau_{\text{sd},\lambda}+\tau_{\text{ss},\lambda}\alpha_\lambda\rho_{\text{dd},\lambda})} \tag{10}$$

3 大气上行、下行辐射分量参数化

3.1 大气辐射分量计算方法

MODTRAN(moderate resolution atmospheric transmittance and Radiance code)是由美国光谱科技公司、空军物理实验室联合利用 FORTRAN 编写的适用计算 0.2μm—∞区间内的大气辐射传输模式(Berk 等, 2000)。从 1989 年至今, MODTRAN 逐步将大气辐射传输方面的最新成果融入到程序中来，版本已经发展到 4。在 MODTRAN 4 中，改进了瑞利散射和复折射指数的计算精度，增加了 DISORT 考虑用多流近似求解辐射传输模型，并且将多种 BRDF 模型引进到模型中，使地表特性的参数化输入成为可能。MODTRAN4 还对几个重要的基础数据库加以更新，改进了高层大气的处理，使计算的精度得到很大提高。MODTRAN4 是目前应用最为广泛精度较高的辐射传输模型(Aires 等, 2002; Ellicott 等, 2009; Verhoef & Bach, 2003)。

利用公式(6)和 MODTRAN4 模型输出结果可以求得 E^{+}(b)、E^{-}(b)和 Q 中 3 个大气参数 $\tau_{\text{ss},\lambda}$、$\tau_{\text{sd},\lambda}$和 $\rho_{\text{dd},\lambda}$。同样将地表假定为均一朗伯体, (6)式变为:

$$\begin{aligned} r_{p,\lambda} &= \rho_{\text{so},\lambda} + && \text{(a)}\\ &\tau_{\text{do},\lambda}\alpha_\lambda\frac{(\tau_{\text{ss},\lambda}+\tau_{\text{sd},\lambda})}{1-\alpha_\lambda\rho_{\text{dd},\lambda}}+ && \text{(b)}\\ &\tau_{\text{oo},\lambda}\alpha_\lambda\frac{(\tau_{\text{sd},\lambda}+\tau_{\text{ss},\lambda}\alpha_\lambda\rho_{\text{dd},\lambda})}{1-\alpha_\lambda\rho_{\text{dd},\lambda}}+ && \text{(c)}\\ &\tau_{\text{oo},\lambda}\alpha_\lambda\tau_{\text{ss},\lambda} && \text{(d)} \end{aligned} \tag{11}$$

设定α_λ分别取值为 0、50%和 100%，根据气象观测数据输入 MODTRAN 4 模型大气参数，利用模型进行三次计算结果即可求解出 3 个大气参数。为方便将 MODTRAN 4 模型输出结果用于方程求解，通过修改 MODTRAN 4 模型程序将与(a)、(b)、(c)及(d)相关的辐射分量直接存储为单独文件。MODTRAN 4 输出 tape7 文件中列数据标识、MODTRAN 4 模型变量及公式(6)对应关系分别为: (1) 大气层顶反射辐射与大气上行漫射辐射之和为‘SOL SCAT’→‘SUMSSR’→(a)+(b); (2) 地表反射太阳直射辐射为‘DRCT RFLT’→‘RFLSS’→(d); (3)地表反射太阳直射和大气下行漫射辐射之和为‘GRND RFLT’→RFS URF’→(c)+(d)。根据上述关系可以得出:

$$L_{(a)+(b)}=[\rho_{\text{so},\lambda}+\tau_{\text{do},\lambda}\alpha_\lambda\frac{(\tau_{\text{ss},\lambda}+\tau_{\text{sd},\lambda})}{1-\alpha_\lambda\rho_{\text{dd},\lambda}}]\frac{E_{\text{s}}(t)}{\pi}\cos\theta_{\text{s}} \tag{12}$$

$$L_{(c)+(d)}=[\tau_{\text{oo},\lambda}\alpha_\lambda\frac{(\tau_{\text{sd},\lambda}+\tau_{\text{ss},\lambda})}{1-\alpha_\lambda\rho_{\text{dd},\lambda}}]\frac{E_{\text{s}}(t)}{\pi}\cos\theta_{\text{s}} \tag{13}$$

$$L_{(d)}=\tau_{\text{oo},\lambda}\alpha_\lambda\tau_{\text{ss},\lambda}\frac{E_{\text{s}}(t)}{\pi}\cos\theta_{\text{s}} \tag{14}$$

其中 $L_{(a)+(b)}$、$L_{(c)+(d)}$、$L_{(d)}$分别为 MODTRAN 4 模型输出的波长λ处辐射分量值。

(1) 假设直射透过率$\tau_{\text{oo},\lambda}$和$\tau_{\text{ss},\lambda}$满足 Beer 定律，则得到:

$$\tau_{\text{oo},\lambda}=\exp(-b/\cos\theta_{\text{o}}),\tau_{\text{ss},\lambda}=\exp(-b/\cos\theta_{\text{s}}) \tag{15}$$

其中 b 为整层大气光学厚度, θ_{o}为传感器观测天顶角, θ_{s} 为太阳入射天顶角。除较强水汽吸收波段可能导致误差较大外，通常大气窗口波段采用 Beer 定律可以满足精度要求。利用(14)和(15)式，当α_λ= 100%时，可得:

$$\begin{aligned}\tau_{\text{oo},\lambda}\tau_{\text{ss},\lambda}&=\exp[-b(1/\cos\theta_{\text{s}}+1/\cos\theta_{\text{o}})]\\ &=L_{(d)}{}^{100}\times\pi/(E_{\text{s}}(t)\cos\theta_{\text{s}})\end{aligned} \tag{16}$$

求得:

$$\begin{aligned}b=-\ln[L_{(d)}{}^{100}\times\pi/(E_{\text{s}}(t)\cos\theta_{\text{s}})]/\\ (1/\cos\theta_{\text{s}}+1/\cos\theta_{\text{o}})\end{aligned} \tag{17}$$

根据 b 值和(15)式可直接求出$\tau_{\text{ss},\lambda}$。

(2) 当α_λ=50%和α_λ=100%时，对于(13)式存在:

$$\begin{cases}\tau_{\text{oo},\lambda}\times0.5\dfrac{(\tau_{\text{sd},\lambda}+\tau_{\text{ss},\lambda})}{1-0.5\rho_{\text{dd},\lambda}}=L_{(\text{c})+(\text{d})}{}^{50}\times\pi/(E_{\text{s}}(t)\cos\theta_{\text{s}})\\ \tau_{\text{oo},\lambda}\dfrac{(\tau_{\text{sd},\lambda}+\tau_{\text{ss},\lambda})}{1-\rho_{\text{dd},\lambda}}=L_{(\text{c})+(\text{d})}{}^{100}\times\pi/(E_{\text{s}}(t)\cos\theta_{\text{s}})\end{cases} \tag{18}$$

可以直接解出$\rho_{\text{dd},\lambda}$为:

$$\rho_{\text{dd},\lambda}=\frac{L_{(\text{c})+(\text{d})}{}^{100}-2\times L_{(\text{c})+(\text{d})}{}^{50}}{L_{(\text{c})+(\text{d})}{}^{100}-L_{(\text{c})+(\text{d})}{}^{50}} \tag{19}$$

(3)取α_λ=100%，联立式(13)和式(14)，可得出:

$$\tau_{\text{sd},\lambda}=[L_{(c)+(d)}{}^{100}(1-\rho_{\text{dd},\lambda})/L_{(d)}{}^{100}-1]\tau_{\text{ss},\lambda} \tag{20}$$

3.2 大气辐射分量分析

Vermote 等(2002)在进行 MODIS 数据可见光-中红外波段的大气订正时，建立的水汽吸收和气溶胶散射相互耦合简化校正模型达到了较高的处理精度。在较短时期内影响大气对短波辐射的影响主要来自水汽和气溶胶的状况；而其他气体或痕量气体变化较小，其对辐射传输过程的影响是相对稳定的。杨贵军等(2007, 2008, 2009)在大气辐射传输邻近效应分析过程中，也得出影响邻近效应的主要大

气因子为水汽含量和能见度。当然，在可见光-近红外波段太阳入射天顶角也是影响大气辐射传输路径长度的关键几何因子。利用 TIGR 大气廓线数据库中晴空条件下的 1413 条大气廓线数据，统计了气柱内水汽含量的变化，分布范围为 0—8.0 g/cm^2，其中 60%廓线水汽含量集中在 1.0(g/cm^2)左右；大气能见度距离参考 Liang 等(2001)给出的取值范围 0.1—35 km；太阳入射天顶角根据 Landsat 5 TM 卫星过境时间和地理位置计算出范围为 0—70°，选择 1976 美国标准大气模式，具体参数设置如表 1 所示，通过改变水汽含量、能见度距离及太阳入射天顶角 3 个变量进行统计分析；其中卫星为天顶向下垂直观测，水汽含量 1.0 g/cm^2、能见度距离 25.0 km 和太阳入射天顶角 30.0°为参数默认值。

表 **1** 输入参数组合

水汽含量/(g/cm^2)	能见度距离/km	太阳入射天顶角/(°)
1.0	0.1	0
2.0	0.5	10.0
3.0	1.0	20.0
4.0	5.0	**30.0**
5.0	10.0	40.0
6.0	15.0	50.0
7.0	**25.0**	60.0
8.0	35.0	70.0

3.2.1 不同水汽条件下参数计算结果

大气中水汽在可见光-近红外波段范围内，主要吸收中心有 0.94、1.1、1.38 和 1.87μm 等波长处。从图 2 看出，即使在水汽含量动态范围变化从 1.0—8.0g/cm^{2}时，单独由于水汽量变化导致的 3 个大气参数变化并不明显，随水汽含量增大有略微减小，变幅仅为 5%左右。其原因是除上述水汽吸收带外，大气中水汽只在波长较长处产生微弱的瑞利散射(>1.0 μm)，其近红外谱区吸收 50%太阳能量。水汽吸收带主要集中在热红外波段，水汽含量越大吸收越严重。所以在热红外遥感中水汽是重要的影响因素，而在可见光-近红外波段范围内水汽的影响要小很多。图中箭头所指方向向下表示与水汽含量增大呈负相关，反之则正相关，以下其他图均为相同含义。

3.2.2 不同气溶胶能见度计算结果

可见光-近红外波段范围内气溶胶产生的米散射非常显著，当大气能见度距离在 0.1—35.0 km 区间变化时，对应 550 nm 处的表层气溶胶消光距离为 39.1—0.1 km^{-1}，由此导致相应大气参数最大变化幅度达到 10 倍左右，如图 3，其中$\tau_{ss,\lambda}$、$\tau_{sd,\lambda}$随能见度距离增大而增大，但$\rho_{dd,\lambda}$则相反减小。其原因是随着能

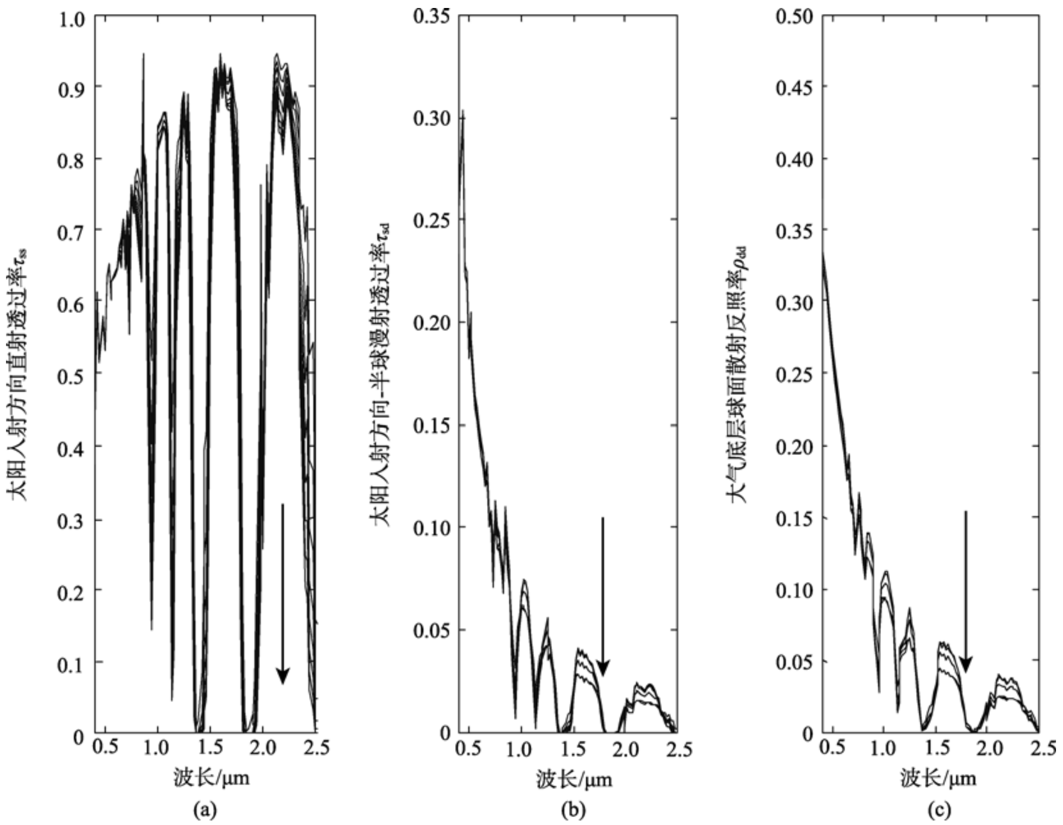

图 2 不同水汽含量条件下大气参数计算结果

(a) 太阳入射方向直射透过率 τ_{ss}; (b) 太阳入射方向-半球漫射透过率 τ_{sd}; (c) 大气底层球面散射反照率 ρ_{dd}

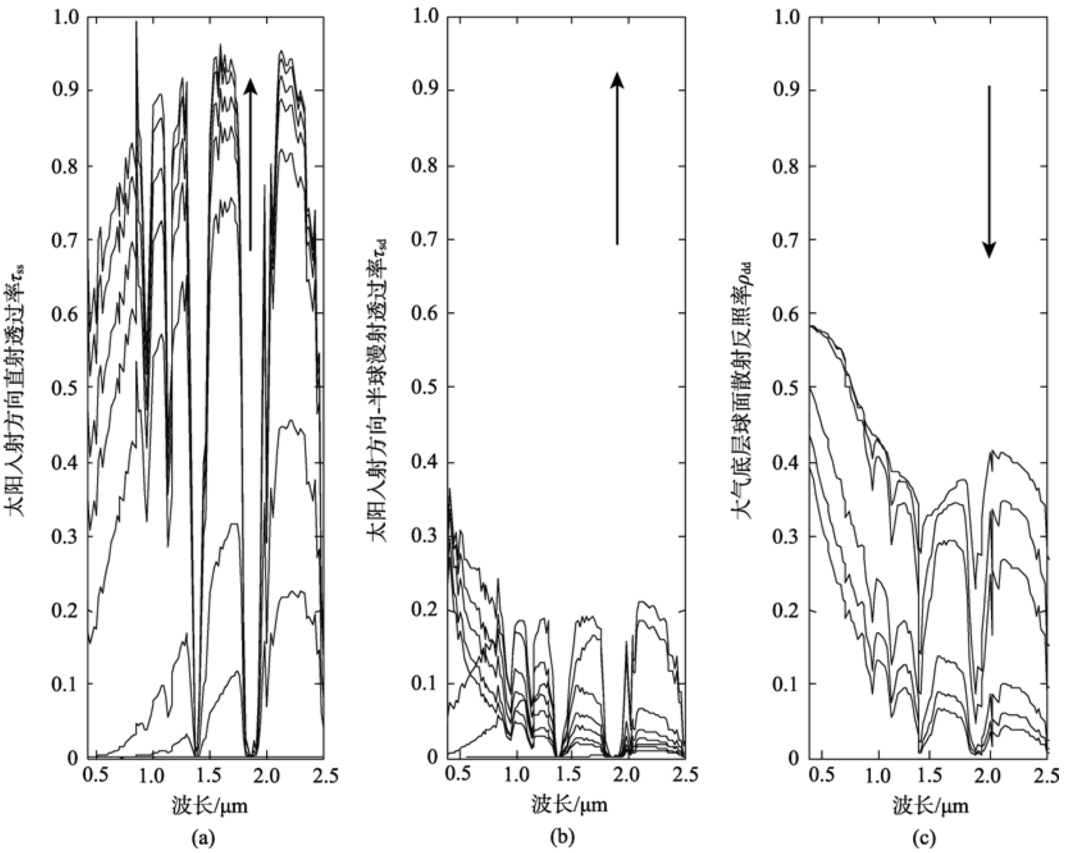

图 3 不同大气能见度距离下大气参数计算结果

(a) 太阳入射方向直射透过率 τ_{ss}; (b) 太阳入射方向-半球漫射透过率 τ_{sd}; (c) 大气底层球面散射反照率 ρ_{dd}

见度距离增大，气溶胶导致的多次散射概率减小，直接增大了大气整层直射和散射透过率，但也同时降低了大气上行漫射辐射与下行漫射辐射间半球-半球方向多次散射的几率，导致$\rho_{dd,\lambda}$呈相反下降趋势。

3.2.3 不同太阳入射天顶角计算结果

当入射太阳天顶角从 0—70°变化时，导致了太阳光线在大气层中传输距离的增加，随着角度增大$\tau_{ss,\lambda}$逐渐减小，变化幅度达到 10 倍左右，如图 4，太阳入射天顶角改变对直射光透过率影响最为显著；相反，$\tau_{sd,\lambda}$随着角度增大而增大，但增大幅度很小；而$\rho_{dd,\lambda}$与太阳入射天顶角大小无关，保持不变。其原因是随着天顶角增大，在直射光传输路径增加的同时，传输过程中发生多次散射的概率有一定增加，但由于相同的大气条件下多次散射增加不会很多，故$\tau_{sd,\lambda}$略微增大。对于$\rho_{dd,\lambda}$来说，其本身只与大气状况相关，与太阳入射和观测方向均无关，代表的是大气层半球-半球方向散射反照率，所以不受太阳入射天顶角变化影响。

3.3 大气上行、下行辐射分量参数化

以 LandSat5 TM 数据为例，其 6 个可见光-近红外波段波长分布范围为 0.4—2.5μm，依次命名为 L5B1, L5B2, L5B3, L5B4, L5B5 及 L5B7，分别代表对应的 Land Sat5 卫星的 1, 2, 3, 4, 5, 7 波段，如图 5，与前面分析的大气上行、下行辐射光谱范围一致，可以直接应用于 TM 数据大气影响计算。

采用下面公式对计算出的原始$\tau_{ss,\lambda}$、$\tau_{sd,\lambda}$和$\rho_{dd,\lambda}$值进行通道积分后，才能得到对应 TM 波段值:

$$\tau_i = \frac{\int \tau(\lambda)\phi_i(\lambda)\mathrm{d}\lambda}{\int \phi_i(\lambda)\mathrm{d}\lambda} \tag{21}$$

其中τ_i为 TM 波段响应积分后的$\tau_{ss,\lambda}$、$\tau_{sd,\lambda}$和$\rho_{dd,\lambda}$值；$\phi_i(\lambda)$为 TM 各波段响应值。

利用非线性最小二乘方法，对 Landsat5 TM 6 个波段积分后结果进行了回归分析，发现 3 个大气参数τ_{ss}、τ_{sd}及ρ_{dd}具有大致相同形式的回归方程，只是在不同波长处存在不同比例缩放因子，最终得到了 3 个大气参数在各波段的拟合结果，如表 2。拟合方程的形式为:

$$\begin{aligned} \text{Fit\_Function} = {} & P_1 * w^3 + P_2 * w^2 + P_3 * w + && \text{(a)} \\ & (P_4 * v + P_5)/(v + P_6) + && \text{(b)} \quad (22) \\ & P_7 * s^2 + P_8 * s && \text{(c)} \end{aligned}$$

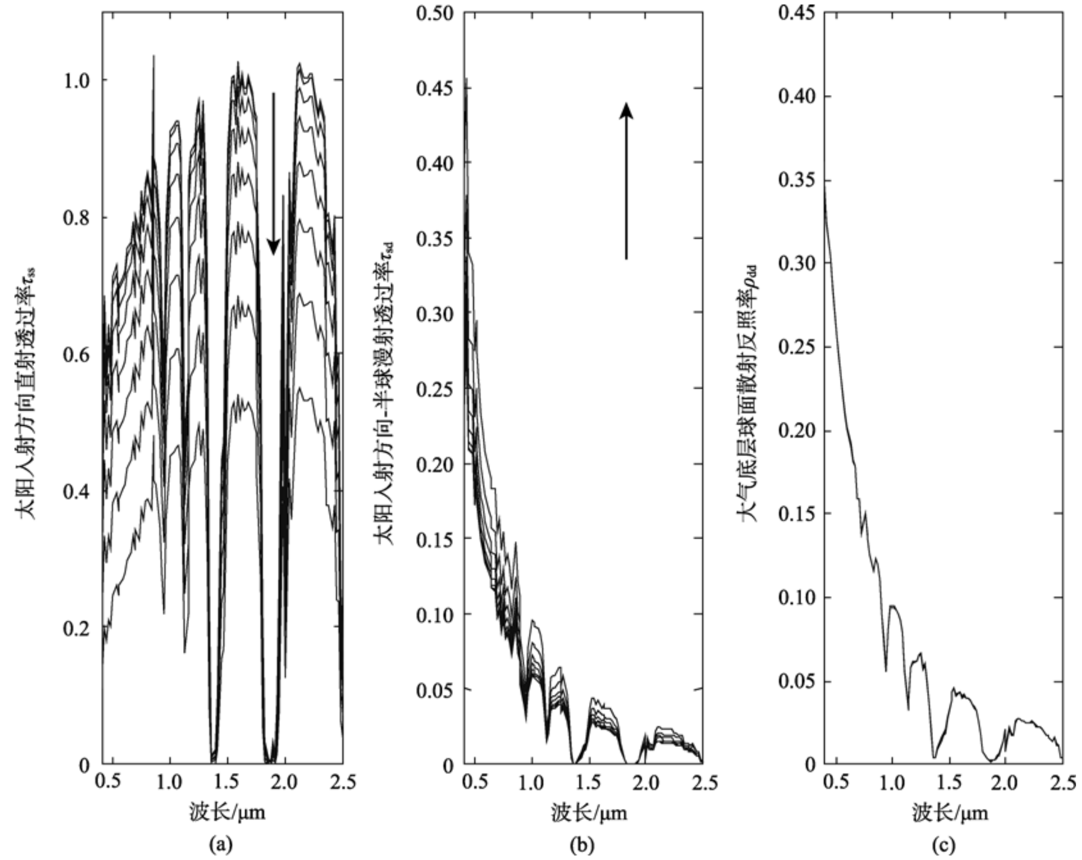

图 4　不同太阳入射天顶角下大气参数计算结果

(a) 太阳入射方向直射透过率 τ_{ss}; (b) 太阳入射方向-半球漫射透过率 τ_{sd}; (c) 大气底层球面散射反照率 ρ_{dd}

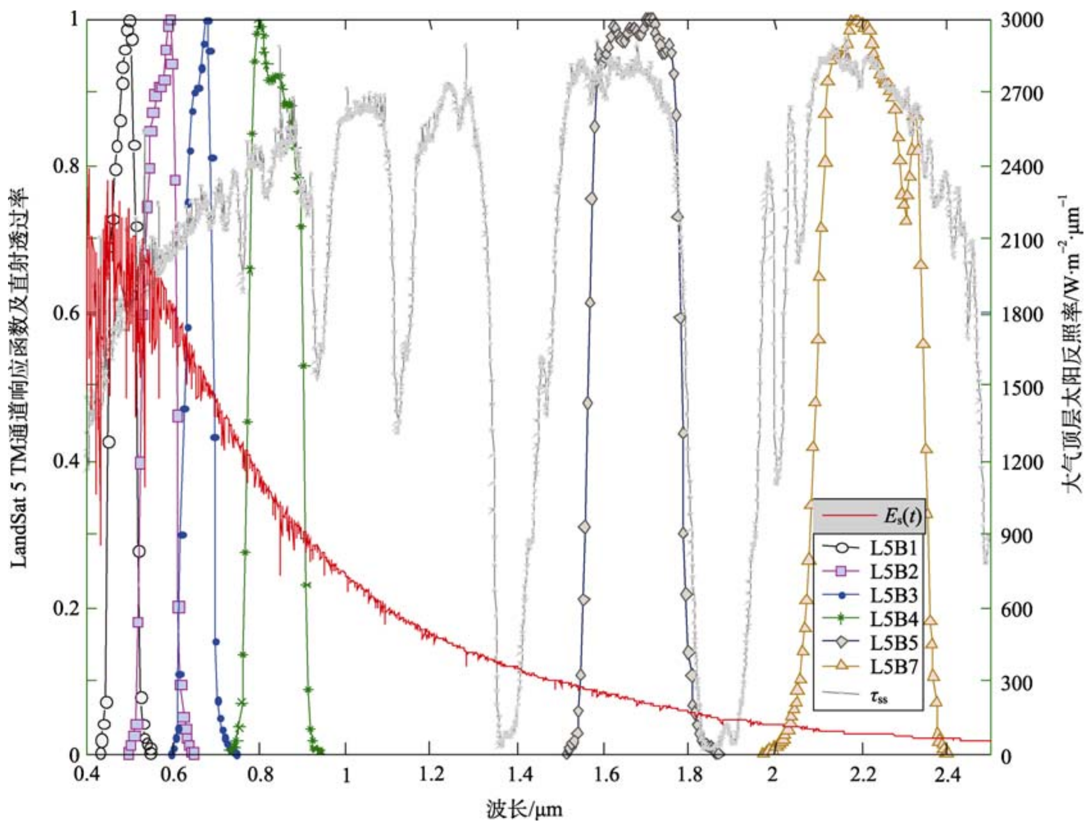

图 5　LandSat 5 TM 波段设置、大气透过率及大气顶层太阳辐照度

表 2 大气参数拟合方程系数及精度评价结果

大气参数	波段号	大气水汽含量 w/(g/cm^2)			水平气象能见度距离 v/km			入射天顶角余弦 s		评价指标			
		P_1	P_2	P_3	P_4	P_5	P_6	P_7	P_8	E	RMSE	Mean bias	Precision
τ_{ss}	L5B1	-7.3020×10^{-5}	0.000902	−0.002000	0.283153	−10.136593	14.789664	−0.215574	0.924471	0.976668	0.007494	6.4740×10^{-12}	0.006188
	L5B2	1.6943×10^{-5}	−0.000195	0.000193	0.248674	−8.024970	10.849285	−0.249366	0.999136	0.979478	0.007597	1.1000×10^{-13}	0.006273
	L5B3	8.8840×10^{-5}	−0.000969	−0.001105	0.237893	−6.201035	7.923271	−0.272271	1.048734	0.979788	0.008429	-5.9850×10^{-12}	0.006960
	L5B4	1.0636×10^{-4}	−0.000624	−0.012719	0.242095	−4.023436	4.770824	−0.289582	1.098384	0.977383	0.009717	-1.1850×10^{-12}	0.008023
	L5B5	1.2605×10^{-4}	−0.000734	−0.017713	0.237681	−1.085536	1.124253	−0.263949	1.052227	0.988499	0.002578	2.3000×10^{-14}	0.002128
	L5B7	1.8587×10^{-4}	−0.002243	−0.007383	0.220485	−0.671325	0.635326	−0.261631	1.058064	0.987215	0.002570	-2.1700×10^{-13}	0.002122
τ_{sd}	L5B1	-6.5944×10^{-5}	0.000733	−0.000932	0.206946	21.899567	40.045200	0.183014	−0.409750	0.934833	0.002992	3.3259×10^{-11}	0.002412
	L5B2	-9.6375×10^{-5}	0.001142	−0.002230	0.157521	9.573606	19.666934	0.117804	−0.274629	0.958120	0.001750	3.2220×10^{-12}	0.001411
	L5B3	-1.2613×10^{-4}	0.001556	−0.004225	0.134619	5.953097	12.565856	0.100128	−0.230907	0.964484	0.001345	3.7000×10^{-13}	0.001084
	L5B4	-1.7901×10^{-4}	0.002297	−0.007375	0.099535	3.364813	7.942021	0.075218	−0.170346	0.964019	0.001161	4.6300×10^{-13}	0.000936
	L5B5	-1.5810×10^{-4}	0.001989	−0.005414	0.026680	0.764273	3.172737	0.020292	−0.046238	0.952023	0.000750	1.0000×10^{-15}	0.000605
	L5B7	-1.2722×10^{-4}	0.001587	−0.004247	0.015071	0.486015	2.376663	0.011527	−0.026883	0.951897	0.000582	-6.6000×10^{-14}	0.000469
ρ_{dd}	L5B1	-1.2526×10^{-4}	0.001448	−0.002485	0.132588	6.431340	10.446559	−0.001434	0.002890	0.990090	0.000960	-2.1000×10^{-14}	0.000784
	L5B2	-1.6153×10^{-4}	0.001932	−0.003977	0.080067	5.640540	9.371051	−0.001711	0.003311	0.982672	0.001045	1.0800×10^{-13}	0.000842
	L5B3	-2.0551×10^{-4}	0.002564	−0.007025	0.051947	4.769732	8.249795	−0.000659	0.001250	0.981714	0.001147	2.2800×10^{-13}	0.000924
	L5B4	-2.7906×10^{-4}	0.003577	−0.011035	0.028184	3.393486	6.895959	0.000224	−0.000571	0.975207	0.001395	-1.0000×10^{-15}	0.001125
	L5B5	-2.5608×10^{-4}	0.003223	−0.008834	0.003741	1.118045	3.871966	−0.000778	0.001295	0.959719	0.001173	-7.8000×10^{-14}	0.000946
	L5B7	-2.1060×10^{-4}	0.002627	−0.007135	0.000269	0.769926	3.011455	−0.001128	0.001866	0.955932	0.000944	9.1000×10^{-14}	0.000761

其中 P_1–P_8 为方程系数项；w, v, s 分别为大气水汽含量(g/cm^2)，水平气象能见度距离(km)及太阳入射天顶角余弦值($\cos\theta_s$)。3 个大气参数与水汽含量、太阳入射天顶角余弦分别呈三次、二次多项式形式；与能见度距离呈一阶有理函数形式。

拟合结果精度评价采取以下指标(郑伟等, 2004; 何立明 等, 2005; 李庆利 等,2006):

(1) 均方根误差(RMSE)，代表了模型估计值与实际观测值间的误差整体分布：

$$\mathrm{RMSE}=\sqrt{\frac{\sum_{i=1}^{n}(e_i-o_i)^2}{n}} \tag{23}$$

式中 e_i, o_i 分别为模型估计值和观测值。

(2) 平均偏差-Mean bias，代表模型估计与实际观测数据总体样本间误差大小：

$$\text{Mean bias}=B=\frac{\sum_{i=1}^{n}(e_i-o_i)}{n} \tag{24}$$

(3) 精度-Precision，表示建立的拟合模型重复性估计精度，即利用平均偏差校正后的标准差，

$$\text{Precision}=\sqrt{\frac{\sum_{i=1}^{n}(e_i-o_i-B)^2}{n-1}} \tag{25}$$

(4) Nash-Sutcliffe 效率系数(E)，其优点在于一方面能表达常用的决定系数 R^2 所代表估计值和观测值样本整体误差一致性大小外，还能充分表示出样本内部误差分布一致性，其取值范围$-\infty$~1, E=1.0 代表模型估计值与观测值完全一致；E=0 代表模型估计值精度可达到观测值平均水平；E<0 表示模型估计值误差较大。

$$E=1.0-\frac{\sum_{i=1}^{n}|e_i-o_i|}{\sum_{i=1}^{n}|e_i-\bar{o}_i|} \tag{26}$$

从表 2 拟合模型精度的统计结果来看，三个大气参数的模型估值精度 E 都达到了 0.95 以上，RMSE 和 Precision 最大值不超 1%，平均偏差比前者小 9 个数量级，所以建立的回归拟合模型具有足够精度，能够准确表示在不同水汽含量、能见度距离及太阳入射天顶角下的大气参数值。

3.4 估算 Landsat 5 TM 窄波段大气上行、下行辐射分量

3.4.1 $\dfrac{E^+(b)}{E^-(b)}$ 比值分析

利用上面得到的 3 个大气参数的回归模型，结合 Landsat 5 TM 波段设置，分析 $\dfrac{E^+(b)}{E^-(b)}$，即 Q 值与水汽含量、能见度距离、太阳入射天顶角及地表反射率间关系，如图 6。在相同地表反射率条件下，不同大气水汽含量条件下 Q 值变化并不明显，但随着波长增加比值 Q 呈近似线性增大，其原因是大气辐射传输影响最显著位置是在大气层 10 km 高度以下，根据图 2 可知与 $E^-(b)$ 相关的两个大气参数($\tau_{\mathrm{sd},\lambda}$和 $\rho_{\mathrm{dd},\lambda}$)随水汽含量增大而减小，随波长增大呈明显减小，并导致 $E^-(b)$减小。而在地表朗伯体假设下 $E^+(b)$ 中地表反射特性参数 $\overline{r_{\mathrm{sd}}}$ 和 $\overline{r_{\mathrm{dd}}}$ 却保持不变，理论上二者应该略有增大。所以，最终形成 Q 值始终大于 1 且随波长逐渐增大趋势。L5B1—L5B4 波段 Q 值均小于 4, L5B1、L5B7 达到了 10—16 左右。

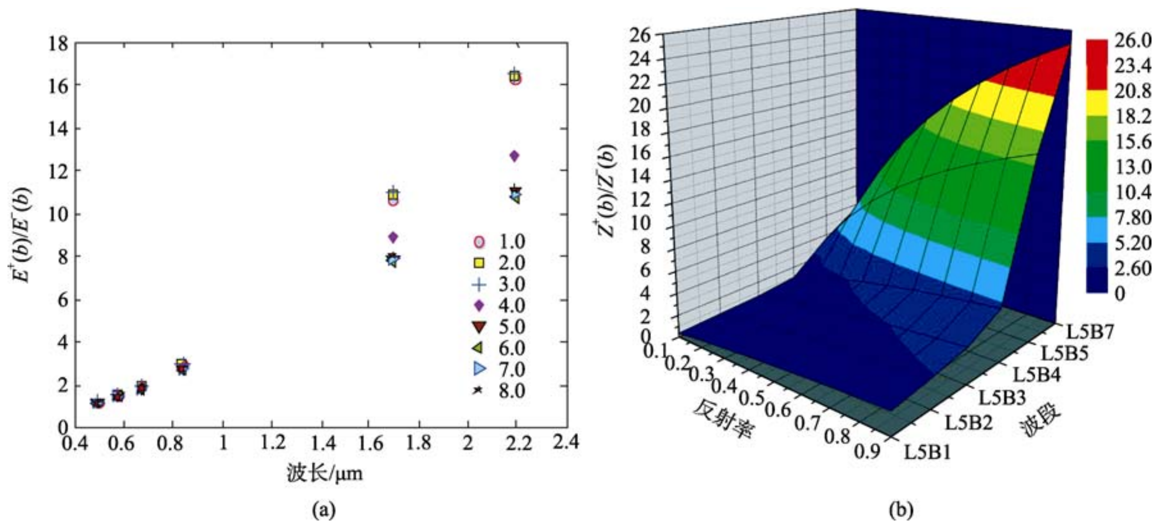

图 6 Q 值与水汽含量和地表反射率关系

(a) 反射率=0.4，含水量=1.0—8.0g/cm^2; (b) 反射率=0.1—0.9，含水量=1.0g/cm^2

从图 6(b)看出, Q 随地表反射率增大时呈现指数性增加，且比值范围进一步扩大到 0.1—25 倍左右，但各波段增大幅度差异较大，其中 L5B1—L5B3 波段均呈现微弱增加，其余 3 个波段增大幅度较大，最高达 26 倍左右。

从图 7 来看, Q 值随波长增加同样呈增大趋势，L5B7 波段处 Q 值最大可达到 L5B1 的 15 倍左右；但随入射太阳天顶角增大而减小，各波段 0—70°太阳入射天顶角下 Q 值呈负指数递减，最大衰减为 0 度的 1/2。对于不同能见度距离条件下 Q 值按波段顺序增大，随能见度距离亦增大，均呈二次多项式形式增大，增大幅度略高于前者，最大达到 22。

3.4.2 估算 TM 窄波段大气上行、下行辐射分量

选择 2009-06-02 北京地区过境 Landsat 5 TM 数据，轨道号(path/row: 123/32)，实验区为北京昌平局部地区，该区内主要地表覆盖类型为冬小麦、裸地及人工建筑。实验区地势平坦，海拔高度 52m。首先根据气象站观测资料估算出试验区水汽含量为 2.82 g/cm^2，能见度距离 22 km，卫星过境时太阳入射天顶角为 33.2°，参考 $\tau_{ss,\lambda}$、$\tau_{sd,\lambda}$和$\rho_{dd,\lambda}$计算方法，利用 MODTRAN 4 三次运行输出结果同样可以计算出公式(11)中其他大气参数，利用定标后的 TM 数据，得到校正后的地表反射率数据，如图 8。

根据 $E^+(b)$、$E^-(b)$和 Q 值计算公式，利用 1 个波数(cm^{-1})分辨率太阳辐照度数据，分别计算出 TM 数据 6 个波段大气上行、下行辐射分量及二者比值，如图 9、图 10。

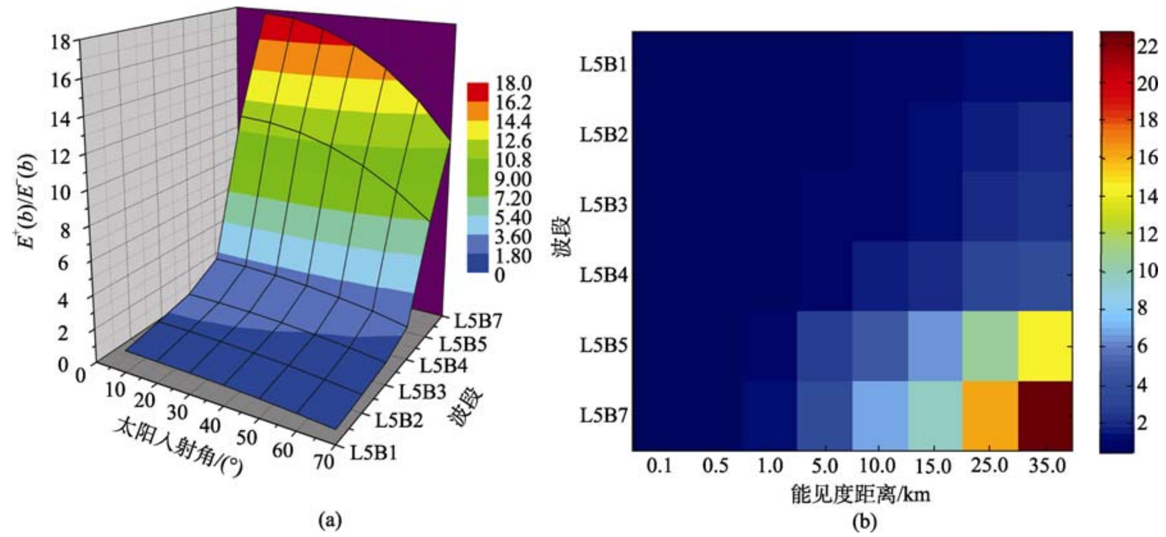

图 7 Q 值与太阳入射天顶角和能见度距离关系, (反射率=0.4)

(a) 不同太阳入射天顶角; (b)不同能见度距离

图 8 Landsat 5 TM 数据反射率数据 (波段组合 R: 7, G: 4, B: 3)

从以上结果可以看出: (1) 在 L5B1 波段植被覆盖区 $E^+(b)$明显低于 $E^-(b)$，$E^-(b)$大致为 430 $W\cdot m^{-2}\cdot\mu m^{-1}$，而$E^+(b)$仅为 45 $W\cdot m^{-2}\cdot\mu m^{-1}$左右，二者相差近 10 倍，这与前面得到结论一致；对非植被覆盖区，$E^+(b)$大致为 100 $W\cdot m^{-2}\cdot\mu m^{-1}$，而 $E^-(b)$仍然大致为 450 $W\cdot m^{-2}\cdot\mu m^{-1}$。表明在该波段植被和裸土区$E^+(b)$差异较大，受地物反射特性影响大；而$E^-(b)$却大致相当，与地表状况相关性小。(2) 在 L5B2 波段$E^+(b)$裸土区大于植被覆盖区，约为 2—3 倍，植被区 $E^+(b)$约为 80 $W\cdot m^{-2}\cdot\mu m^{-1}$；而 $E^-(b)$则与地表覆盖类型相关性较小，植被覆盖区仅低于裸土区 20 $W\cdot m^{-2}\cdot\mu m^{-1}$。(3) 在 L5B3 波段存在与 L5B2 波段大致相同规律，裸土覆盖区 $E^+(b)$为最高，约为 200 $W\cdot m^{-2}\cdot\mu m^{-1}$；

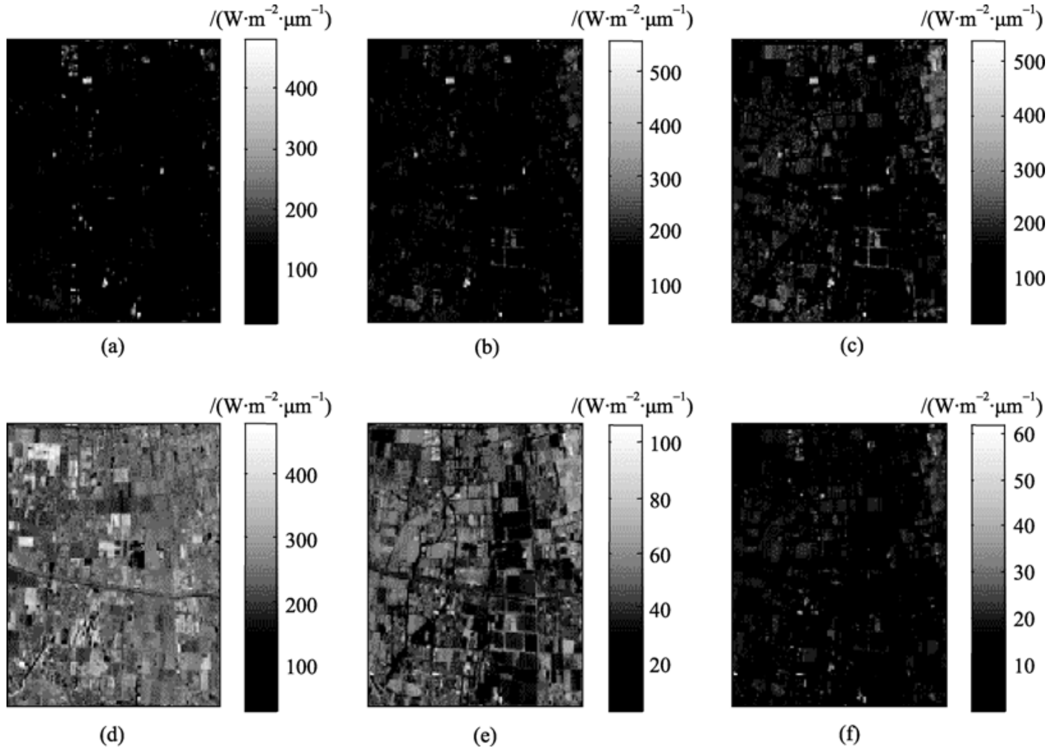

图 9　Landsat 5 TM 6 波段大气上行漫射辐射

(a) L5B1; (b) L5B2; (c) L5B3; (d) L5B4; (e) L5B5; (f) L5B7

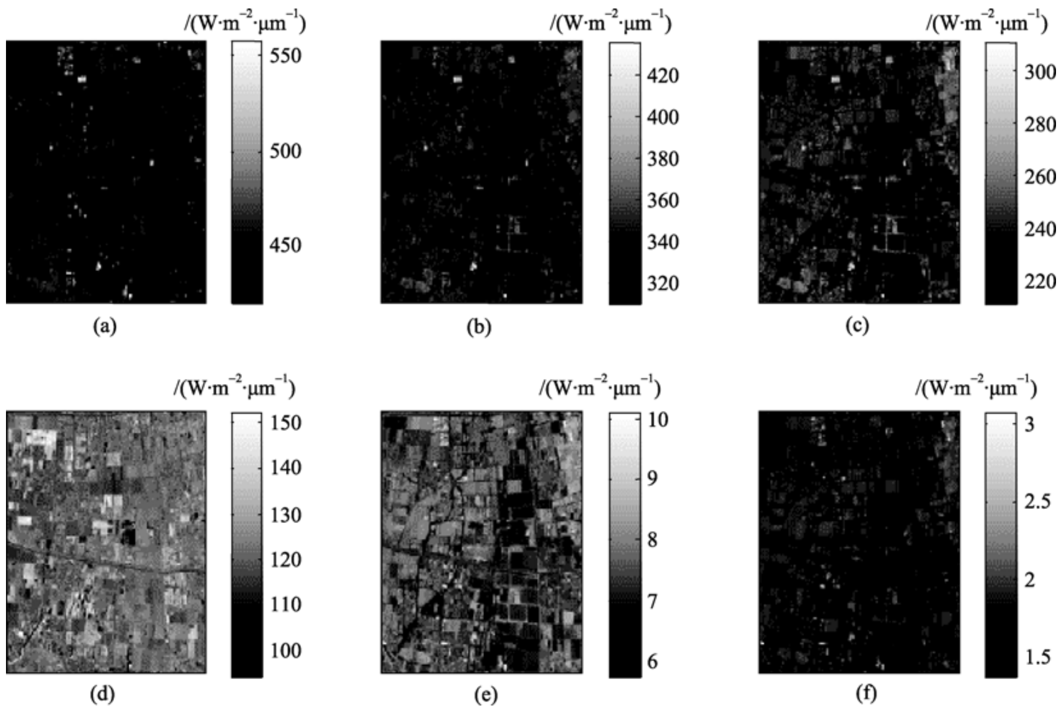

图 10　Landsat 5 TM 6 波段大气下行漫射辐射

(a) L5B1; (b) L5B2; (c) L5B3; (d) L5B4; (e) L5B5; (f) L5B7

$E^{-}(b)$在植被覆盖区仅低于裸土区 30 W·m^{-2}·μm^{-1}。(4) 在 L5B4 波段，$E^{+}(b)$在植被覆盖区高出裸土区 50 W·m^{-2}·μm^{-1}，最高约 250 W·m^{-2}·μm^{-1}；而 $E^{-}(b)$则在两种覆盖区域大致相同，约为 110 W·m^{-2}·μm^{-1}。(5) L5B5 波段 $E^{+}(b)$和 $E^{-}(b)$均明显低于上述 4 个波段，最大降低幅度超过 10 倍；其中 $E^{+}(b)$高于 $E^{-}(b)$ 5 倍左右，但二者受地表覆盖状况影响较小，$E^{+}(b)$约为 40 W·m^{-2}·μm^{-1}。(6) L5B7 波段 $E^{+}(b)$和 $E^{-}(b)$值更

小, $E^-(b)$在植被覆盖和裸土覆盖区大致相同，约为 2 W·m^{-2}·μm^{-1}；而 $E^+(b)$在植被覆盖区为裸土区 1/3 左右，为 7 W·m^{-2}·μm^{-1}。由于 TOA 太阳辐照度从 0.4 μm 后逐渐下降，至波长 2.5μm 处已经降低了约 40 倍，参见图 5，所以 L5B1 至 L5B7 $E^+(b)$和 $E^-(b)$也呈降低趋势。从总体来看，前 3 个波段 $E^+(b)$均低于 $E^-(b)$，而从第 4 波段开始 $E^+(b)$逐渐大于 $E^-(b)$。

3.5 讨 论

文中给出的四流近似大气辐射传输解析模型已成功用于多光谱或高光谱遥感数据的大气校正。为了求解出模型中部分与地表特性无关的大气参数，利用了地表朗伯体假设条件，分别将模型设置在不同的地表反射率下进行联合求解，通过对四流近似解析模型与原始 MODTRAN 4 计算入瞳处总辐射进行比较，即将 MODTRAN 4 模型输出结果看作真值，计算本文模型与 MODTRAN 4 模型的相对误差。结果表明在所有波长处二者相对误差均优于 0.5%，如图 11。同时对上文中列出的$\tau_{ss,\lambda}$、$\tau_{sd,\lambda}$和$\rho_{dd,\lambda}$ 3 个参数与 Verhoef 等(2003)计算结果进行了对比，从参数数值范围及精度方面完全一致。

本文提供的大气辐射传输四流近似简化解析方法，目的之一是用于遥感成像模拟，在进行大气辐射分量分析、参数化及利用 Landsat 5TM 进行大气上行、下行辐射计算时，仍然假设地表为朗伯体，故而式(6)可变换成式(11)，式(7)—式(9)可转换为式(10)，其内在隐含着地表邻近效应作用尺度与地物空间尺度相同，即将式(3)中的$\overline{r_{sd}}$及$\overline{r_{dd}}$两项对应的邻近地物假定为与目标地物具有相同反射率的朗伯体。这样处理的后果是在计算 Landsat 5 TM 每个像元的大气上行、下行辐射时，像元被看成均一无限大的朗伯表面，此时邻近效应作用达到极大，且保持与像元相同分辨率。当然这是式(3)的一种典型情况，例如在相对均一的大面积水体、沙漠等地表时式(10)、式(11)是成立的。如果考虑邻近效应(胡宝新等，1996；牛铮等，1997；肖青等，2005)，应在地表朗伯体假设条件下计算出$\tau_{ss,\lambda}$、$\tau_{sd,\lambda}$和$\rho_{dd,\lambda}$ 3 个参数后，对$\overline{r_{sd}}$及$\overline{r_{dd}}$应该利用不同地物辐射传输模型直接或利用大气点扩散函数(PSF)间接计算出二者大小。初步估算表明在本文使用 Landsat 5 TM 对应 22 km 水平气象能见度距离条件下，二者造成的邻近效应贡献约为 5%左右。所以本文中计算的像元上的大气上行、下行辐射只能表达在像元尺度上二者

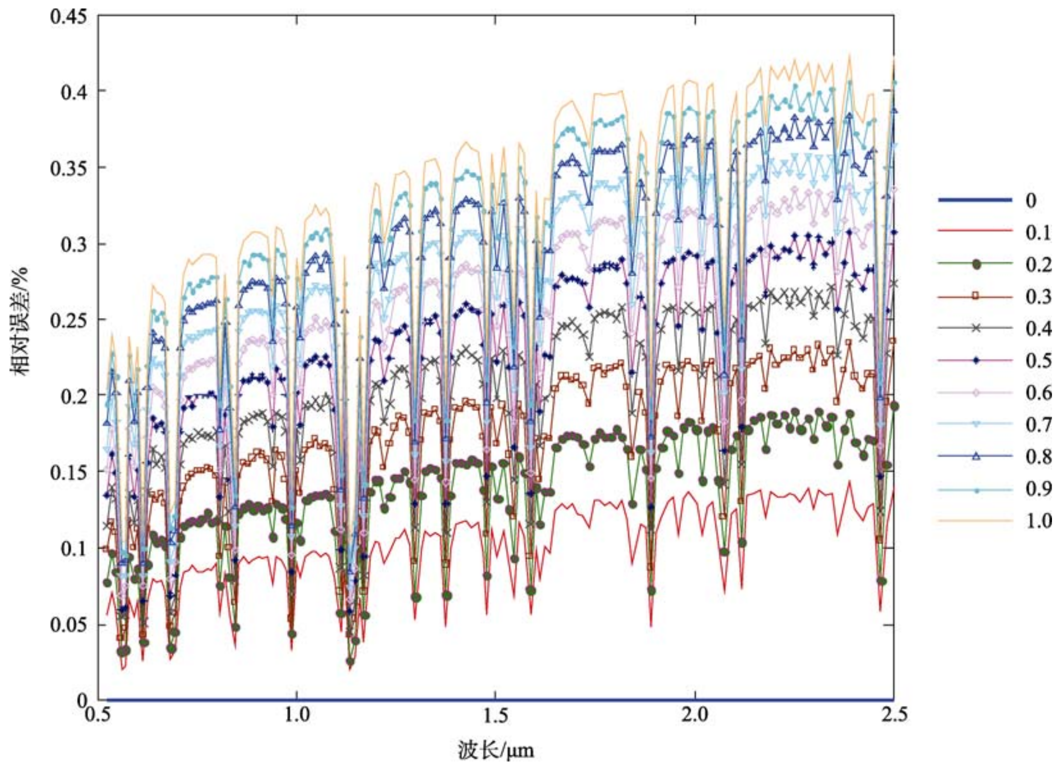

图 11 大气辐射传输解析模型误差分析(反射率: 0—1.0)

的数量级大小，精确的计算需要考虑不同地物对应的邻近效应影响尺度和量级是不同的，也就是由于 $\overline{r_{sd}}$ 及 $\overline{r_{dd}}$ 产生的邻近效应会使 $E^{+}(b)$呈现不同程度的低通滤波后的模糊效果，进而也影响到 $E^{-}(b)$。考虑到本文目标之一是应用大气辐射传输解析模型用于遥感成像模拟，评价理想条件下传感器响应特性；后续工作中将利用光线追踪方法近似计算邻近效应，求出每个像元对应的 PSF 大小及空间范围，计算出符合实际情况的大气上行、下行辐射分量。

4 结 论

本文根据四流辐射传输理论，建立了可见光-近红外波段大气辐射传输数值模型，考虑了传感器入瞳处大气上行、下行漫射反射贡献。通过利用 MODTRAN 4 模型对与二者相关的大气参数进行了计算，得到了太阳直射方向大气透过率$\tau_{ss,\lambda}$、太阳光线方向至半球漫射透过率$\tau_{sd,\lambda}$及 BOA 处大气半球漫射反照率$\rho_{dd,\lambda}$等 3 个大气参数。通过分析确定影响 3 个大气参数的主要因子为大气水汽含量、气象能见度距离和太阳入射天顶角。利用 TIGR 大气廓线库分析得到 60%水汽含量为 1.0 左右，范围为 0.1—8.0 g/cm^2 左右；能见度距离取值为 0.1—35 km；太阳入射天顶角 0—70°，根据上述参数的取值范围和不同组合，对 3 个大气参数的敏感性进行了分析，得出了以下主要结论: (1) 水汽含量变化导致的 3 个大气参数变化并不明显，随水汽含量增大有略微减小，变幅仅为 5%左右；(2) 不同气溶胶能见度导致 3 个大气参数最大变化幅度达到 10 倍左右。$\tau_{ss,\lambda}$、$\tau_{sd,\lambda}$随能见度距离增大而增大，但$\rho_{dd,\lambda}$则相反减小；(3) 随着太阳入射天顶角增大 $\tau_{ss,\lambda}$逐渐减小，变化幅度达到 10 倍左右，相反$\tau_{sd,\lambda}$随着角度增大而增大，但增大幅度很小；而$\rho_{dd,\lambda}$与太阳入射天顶角大小无关，保持不变。

此外，对 3 个大气参数进行回归分析发现具有相同的参数化形式，其中 3 个大气参数与水汽含量、太阳入射天顶角余弦分别呈三次、二次多项式形式；与能见度距离呈一阶有理函数形式。3 个大气参数的模型估值精度 E 达到了 0.95 以上，最大 RMSE 和 Precision 均小于 1%，证明所建立的参数化模型具有很好精度。另外针对 Landsat 5 TM 6 个窄波段进行了大气上行、下行漫射辐射计算，得出不同大气水汽含量条件下 Q 值变化并不明显，但随着波长增加比值 Q 呈近似线性增大，与 TOA 处大气辐照度减小相反；Q 随大气水汽含量、气象能见度距离和太阳入射天顶角呈指数性增加，比值范围扩大到 0.1—25 倍左右，但各波段增大幅度差异较大。通过对 TM 各波段大气上行、下行漫射辐射分析发现，$E^{-}(b)$无论在植被或裸土覆盖区均大致相当，但随波段顺序而减小；而 $E^{+}(b)$除在 L5B4 和 L5B5 波段相近外，植被覆盖区 $E^{+}(b)$大约为裸土覆盖区 2—4 倍。

文中大气上行、下行辐射计算是基于地表朗伯体假设完成的，计算出的大气上行、下行辐射是一种理想漫反射条件下的结果，与实际情况有一定区别。此外，对地形、高程影响因素暂时忽略，方法仅适合平坦区域。以上问题将是模型下一步改进的工作重点。

REFERENCES

Abduwasit G, Qin Q M and Zhu L J. 2004. 6S model based atmospheric correction of visible and near infrared data and sensitivity analysis. *Acta Scientiarum Naturalium Universitatis Pekinensis*, **40**(4): 116—816

Aires F, Alain C, Noëlle A S and Rossow W B. 2002. A regularized neural net approach for retrieval of atmospheric and surface temperatures with the IASI instrument. *Journal of Applied Meteorology*, **41**(2): 144—159

Berk A, Anderson G P, Acharya P K, Chetwynd J H, Bernstein L S, Shettle E P, Matthew M W and Adler-Golde S M. 2000. MODTRAN4 Users Manual, Air Force Research Laboratory, Space Vehicles Directorate, Air Force Materiel Command, Anscom AFB, MA 01731—3010

Ellicott E, Vermote E, Petitcolin F and Hook S J. 2009. Validation of a new parametric model for atmospheric correction of thermal infrared data. *IEEE Transactions Geoscience and Remote Sensing*, **47**(1): 295—311

Ghulam Abduwasit, Qin Q M and Zhu L J. 2004. 6S Model based atmospheric correction of visible and near infrared data and sensitivity analysis. *Acta Scientiarum Naturalium Universitatis Pekinensis*, **4**(40): 116—816

Gastellu-Etchegorry J P, Martin E and Gascon F. 2004. DART: A 3D model for simulating satellite images and studying surface radiation budget. *International Journal of Remote Sensing*, **25**: 73—96

He L M, Yan G J, Wang Q and Li X W. 2005. Models and its analysis about the atmospheric correction of optical remote sensing imagery. *Geo-Information Science*, **7**(4): 32—38

Hu B X, Li X W, Zhu C G and Strahler A H. 1996. Deriving the anisotropic atmospheric pointspread function of off-nadir remote sensing. *Journal of Image and Graphics*, (1): 19—29

Kaufman Y J and Sendra C. 1988. Algorithm for automatic atmospheric corrections to visible and near-IR satellite imagery. *International Journal of Remote Sensing*, **9**(8): 1357—1381

Liang S L, Fang H L and Chen M. 2001. Atmospheric correction of landsat ETM+ land surface imagery—Part Ⅰ: methods. *IEEE Trans Geosci Remote Sensing*, **39**: 2490—2498

Liang S L and Fang H L. 2004. An improved atmospheric correction algorithm for hyperspectral remotely sensed imagery. *IEEE Trans Geosci Remote Sensing*, **1**(2): 112—117

Li Q L, Xue Y Q, Wang J Y and Bai Z Q. 2006. Atmospheric correction of PHI hyperspectral imagery. *Journal of Infrared and Millimeter Waves*, **25**(4): 613—913

Nie A X, Zhang L T and Chen Z A. 2007. A practical atmospheric correction method and its application in the hyperion image. *Journal of East China Institute of Technology*, **30**(2): 157—160

Niu Z, Zhu C G and Wang C Y. 1997. Analysis of atmospheric cross radiation in a slant viewing angle. *Journal of Remote Sensing*, **1**(2): 88—93

Qin W and Gerstl S A. 2000. 3-D Scene modeling of semi-desert vegetation cover and its radiation regime. *Remote Sensing of Environment*, **74**: 145—162

Vermote E F, Saleous N Z and Justice C O. 2002. Atmospheric correction of the MODIS data in the visible to middle infrared: first results. *Remote Sensing of Environment*, **83**(1): 97—111

Verhoef W. 1984. Light scattering by leaf layers with application to canopy reflectance modeling: the sail model. *Remote Sensing of Environment*, **16**: 125—141

Verhoef W and Bach H. 2003. Simulation of hyperspectral and directional radiance images using coupled biophysical and atmospheric radiative transfer models. *Remote Sensing of Environment*, **87**: 23—41

Xiao Q, Liu Q H, Li X W, Chen L F and Liu Q. 2005. Analysis and correction of atmospheric cross radiation for high geometric resolution airborne remote sensing data. *Journal of Remote Sensing*, **9**(6): 625—633

Yang G J, Liu Q H, Liu Q, Xiao Q, Gu X F and Huang W J. 2009. Mid-infrared atmosphere radiation transfer analytic model and remote sensing images simulation. *Spectroscopy and Spectral Analysis*, **29**(3): 629—633

Yang G J, Liu Q H, Liu Q, Xiao Q and Gu X F. 2008. Adjacency effect analysis in imaging simulation of high-resolution mid-infrared (3—5μm) remote sensing. *Journal of Infrared and Millimeter Waves*, **27**(3): 1—8

Yang G J, Liu Q H, Huang H G, Liu Q and Gu X F. 2007. Methods for simulating infrared remote sensing imagines based on scene models. *Journal of Infrared and Millimeter Waves*, **26**(1): 1—7

Zheng W and Zeng Z Y. 2004. A review on methods of atmospheric correction for remote sensing images. *Remote Sensing Information*, (4): 66—96

附中文参考文献

阿布都瓦斯提·吾拉木, 秦其明, 朱黎江. 2004. 基于6S 模型的可见光、近红外遥感数据的大气校正. 北京大学学报(自然科学版) , **40**(4): 116—816

何立明, 阎广建, 王桥, 李小文. 2005. 光学遥感大气订正模型及其相关问题分析. 地球信息科学, **7**(4): 32—38

胡宝新, 李小文, 朱重光, Alan Strahler. 1996. 大倾角光学遥感中大气点扩散函数的近似模型. 中国图象图形学报, (1): 19—29

李庆利, 薛永祺, 王建宇, 白智全. 2006. PHI 高光谱图像的大气校正算法. 红外与毫米波学报, **25**(4): 613—913

聂爱秀, 张立亭, 陈竹安. 2007. 大气校正方法及其在高光谱影像. Hyperion 中的应用. 东华理工学院学报, **30**(2): 157—160

牛铮, 朱重光, 王长耀. 1997. 斜视角度下大气交叉辐射影响分析. 遥感学报, **1**(2): 88—93

肖青, 柳钦火, 李小文, 陈良富, 刘强. 2005. 高分辨率机载遥感数据的交叉辐射影响及其校正. 遥感学报, **9**(6): 625—633

杨贵军, 柳钦火, 刘强, 肖青, 顾行发, 黄文江. 2009. 中红外大气辐射传输解析模型及遥感成像模拟. 光谱学与光谱分析, **29**(3): 629—633

杨贵军, 柳钦火, 刘强, 肖青, 顾行发. 2008. 高分辨率中红外遥感(3—5μm)成像模拟中邻近效应分析. 红外与毫米波学报, **27**(3): 1—8

杨贵军, 柳钦火, 黄华国, 刘强, 顾行发. 2007. 基于场景模型的热红外遥感成像模拟方法. 红外与毫米波学报, **26**(1): 1—7

郑伟, 曾志远. 2004. 遥感图像大气校正方法综述. 遥感信息, (4): 66—96